2014

Relating Microstructure to Process Variables in Beam-Based Additive Manufacturing of Inconel 718

John Ryan Thompson
Wright State University

RELATING MICROSTRUCTURE TO PROCESS VARIABLES IN BEAM-BASED ADDITIVE MANUFACTURING OF INCONEL 718

A thesis submitted in partial fulfillment
of the requirements for the degree of
Master of Science in Engineering

By

JOHN RYAN THOMPSON
B.S., Wright State University, 2012

2014

Wright State University

WRIGHT STATE UNIVERSITY

GRADUATE SCHOOL

March 7, 2014

I HEREBY RECOMMEND THAT THE THESIS PREPARED UNDER MY SUPERVISION BY John Ryan Thompson ENTITLED Relating Microstructure to Process Variables in Beam-Based Additive Manufacturing of Inconel 718 BE ACCEPTED IN PARTIAL FULFILLMENT OF THE REQUIREMENTS FOR THE DEGREE OF Master of Science in Engineering.

Nathan W. Klingbeil, Ph.D.
Thesis Director and
Dean of the College of Engineering

Committee on
Final Examination

George Huang, P.E.,Ph.D., Chair
Department of Mechanical and
Materials Engineering

Nathan W. Klingbeil, Ph.D.

Raghavan Srinivasan, P.E., Ph.D.

Jaimie Tiley, Ph.D.

Robert E.W. Fyffe, Ph.D.
Vice President for Research and
Dean of the Graduate School

ABSTRACT

Thompson, John Ryan. M.S., Egr., Wright State University, 2014. *Relating Microstructure to Process Variables in Beam-Based Additive Manufacturing of Inconel 718.*

The advancement of laser or electron beam-based additive manufacturing requires the ability to control solidification microstructure. Previous work combined analytical point source solutions and nonlinear thermal finite element analysis (FEA) to explore the effects of deposition process variables on Ti-6Al-4V solidification microstructure. The current work seeks to extend the approach to Inconel 718, with the addition of Cellular Automaton-Finite Element (CAFE) models. Numerical data from finite element results are extracted in order to calculate accurate melt pool geometry, thus leading to corresponding cooling rates and thermal gradients. The CAFE models are used to simulate grain grown and nucleation, providing a link between additive manufacturing process variables (beam power/velocity) and solidification microstructure. Ultimately, a comparison of results between Ti-6Al-4V and Inconel 718 is expected to lay the ground work for the integrated control of melt pool geometry and microstructure in other alloys.

TABLE OF CONTENTS

LIST OF FIGURES

Page

LIST OF TABLES

Page

Acknowledgements

It gives me great pleasure in expressing my gratitude to all those people who have supported me and had their contribution in making this thesis possible. First and foremost, I must acknowledge and thank God for giving me this opportunity and giving me the discipline to work diligently to earn this degree. I could never accomplish this without the strong faith I have in Christ.

I would like to express deepest appreciation and love to my wife, Shelly Thompson. She was my cheerleader, counselor and drill sergeant at various time throughout this journey – I could not have done this without you my love!

I would like to thank my sons and daughter, Blake, Trent and Paige Thompson. I sacrificed a lot of daddy time to hopefully provide you with a better quality of life. I hope that I have instilled the importance of a higher education to the three of you and I hope you will now understand, "What is dad doing in the basement for a thousand hours!"

I would like to convey my gratefulness to my advisor and friend Dean Nathan Klingbeil. You recognized something in me that I surely did not in my first term at Wright State University. You have given me countless opportunities to shine both in the classroom as a student and as an instructor. I will never forget how you introduced me to the former dean, "This is John Thompson, I believe he is a real diamond in the rough." I truly thank you Dr. K!

Lastly I would like to thank my extended family for understanding the commitment this has been. At times it was as if I was deployed overseas, as I would have to devote so much energy to this work. Thank you all for the support.

Chapter 1. Introduction

1.1 Motivation

Early use of additive manufacturing focused on pre-production prototypes made from simple alloys and polymers. As time progressed, additive manufacturing has begun to fabricate high-end aircraft components, automobile products, and medical implants [1]. With the added sophistication and sensitivity of the products created, predictable and desirable material properties were needed. Ti-6Al-4V was an important alloy to investigate as it is commonly used in both the aerospace and medical fields, industries where consistent and desirable material properties are paramount for design purposes. At this point several things are know about Ti-6Al-4V as it pertains to the additive manufacturing process. A major breakthrough has been the linkage between processing variables (beam power and velocity) and solidification microstructure [2].

This thesis makes similar links between additive manufacturing process variables and solidification microstructure in Inconel® alloy 718. The similarities between Ti-6Al-4V and Inconel 718 solidification maps are the first step in developing integrated control of melt pool geometry and microstructure, which is expected to extend to other alloy systems. This will allow for microstructure control with simple adjustment to beam power and/or beam velocity.

1.2 Literature Review

Additive manufacturing is appropriately named, as it describes the technologies that build 3D objects by adding layer after layer of material, whether the material is plastic, metal

or any other material [1]. In these processes, layers of material are deposited on a substrate or base material to build up geometry in the vertical axis through consecutive layers [3]. Additive manufacturing is ideal for making prototypes during the early development phases of a product, as it significantly reduces the time required for product development, expediting market launches in most cases [4]. Strengths of additive manufacturing lie in areas where conventional manufacturing reaches its limitations, including highly complex structures that require high degrees of design freedom [3, 4]. Companies are beginning to use additive manufacturing in several industries including aerospace, medicine, automotive, special-purpose engineering, and tool making [1, 3, 4]. The additive manufacturing process provides the ability to reduce the material waste resulting from traditional machining practices [5].

The most common form of additive manufacturing is known as 3D printing and has become extremely popular amongst modelers and in academia, with the most common medium being polymers [4]. This thesis will focus on additive manufacturing as it pertains to metallic alloys. Laser engineered net shaping (LENS™) was an example of early beam-based additive manufacturing [6]. The LENS™ process seen in Figure 1.2.1 was developed at Sandia National Laboratories and was made commercially available by Optomec Design Company in 1997 [7]. The LENS™ process used a laser beam along with a powder alloy delivery nozzle to build parts layer-by-layer. Using a laser beam for the additive manufacturing process, the user had capabilities to control beam power and velocity along with powder feed rate of the alloy [8]. When the electron beam free form fabrication (EBF^3) method was introduced, by NASA Langley, more control was given to the user. The user could control beam size and shape, when coupled with an increase of

power absorption, the EBF^3 method became very appealing. The EBF^3 as shown in Figure 1.2.2 has a moving substrate with stationary electron beam heating a wire fed alloy, building geometry layer by layer [8].

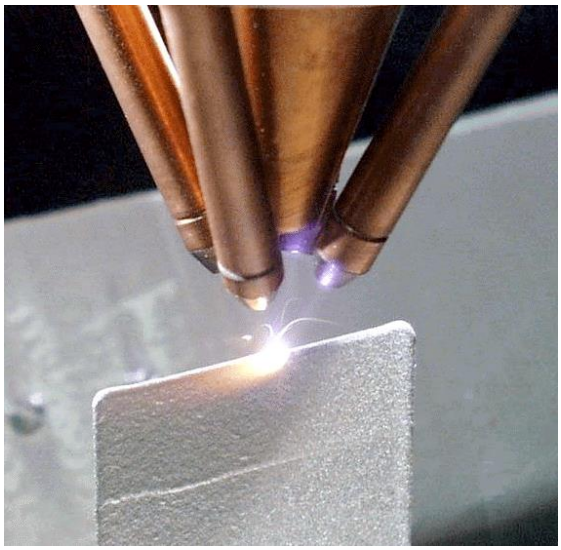

Figure 1.2.1 – LENS™ powder fed process [6]

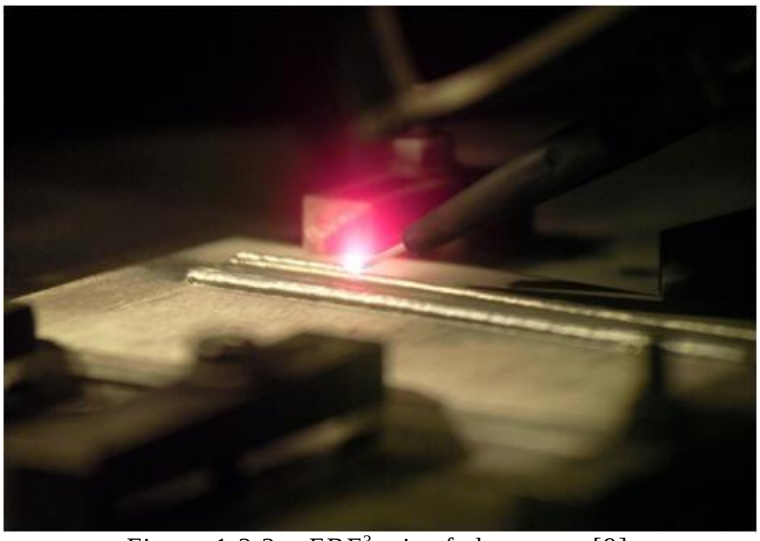

Figure 1.2.2 – EBF^3 wire fed process [9]

Additive manufacturing has continued to advance at an incredible rate and the most popular process today is the Arcam process, which creates parts from metal powders for the biomedical and aerospace industries [10]. An Arcam electron beam powder bed is

shown in Figure 1.2.3. In this process, the powder metal is off to the right; the print head on the left contains the electron beam. As the print head moves the powder across the build tray it creates the desired geometry. Next the print head returns to its starting point and the build tray drops allowing the print head to print the next layer on top of the last.

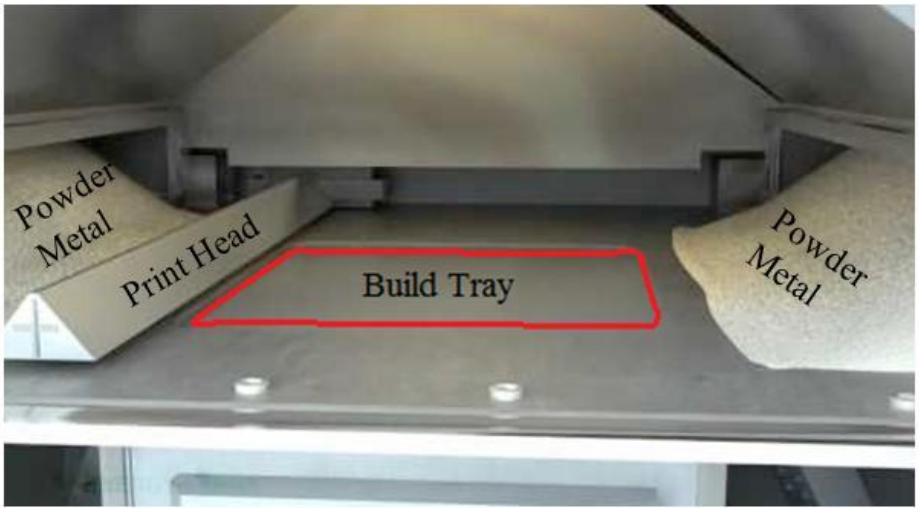

Figure 1.2.3 – Arcam electron beam powder bed process [10]

The aerospace industry has been driving many of the research efforts in the area of additive manufacturing, as there are huge cost savings in the idea of repair verses replace [5, 10]. Not only does the additive manufacturing process have the capabilities to create geometries on a substrate, but it also has the ability to repair existing flawed geometry [8].

With the focus on the aerospace industry, a large portion of current research in additive manufacturing has gone into Ti-6Al-4V. Vasinonta et al. worked with Ti-6Al-4V, who ascertained process variables in dimensionless form [11, 2] as they pertained to the 2D and 3D Rosenthal solution for a moving point hear source. The Rosenthal solution was first used by Dyhuizen and Dobranich to provide analytical solutions for the LENS™ process [12, 13, 14]. Bontha et al. later found the dimensionless thermal conditions

(thermal gradient and cooling rate) governing the solidification microstructure in Ti-6Al-4V [11, 2, 15]. Previously, Brown et al. worked diligently to simulate microstructure in Ti-6Al-4V in casting ingots [16], following the work of Kobryn et al. in classification of grain morphology [17, 18]. Davis et al. continued with the prior authors work, observing the effect of free edges on melt pool geometry in both 2D and 3D geometries of Ti-6Al-4V [6]. More recently, Doak et al. studied the effect of process variables on sub-melt thermal behavior and solid-state phase transformation in beam-based additive manufacturing of Ti-6Al-4V [19]. Davis et al. later established a breakthrough link between melt pool geometry and solidification microstructure [20], laying the groundwork for process mapping for integrated control of both. An overview of the resulting process mapping method for integrated control of melt pool geometry and microstructure is given by Beuth et al. [21]

Up to this point very little work has been done to expand the work in additive manufacturing to other alloy systems. Inconel® alloy 718 (IN718) is used in the aerospace industry in high heat applications. Huang et al. explored the heat-affected zone of IN718 sheet welded with electron-beam welding [22]. Wang et al. looked at the effect of cooling rates on segregation and density variation in the mushy zone during solidification of superalloy IN718 [23]. Nastac et al. showed the advances in the solidification of IN718 and RS5 alloys [24]. However, little is known about IN718 as it pertains to additive manufacturing

1.3 Material

Inconel® is a trademarked name of the Special Metals Corporation group of companies for a series of austenitic nickel-chromium-based super alloys. Specifically, Inconel®

alloy 718 is used for high strength, corrosion sensitive applications, between -423°and 1300° F [25]. Typical composition limits are shown in Table 1.3.1.

Element	Wt. %
Nickel (plus Cobalt)	50.00 - 55.00
Chromium	17.00 - 21.00
Iron	Balance
Niobium (plus Tantalum)	4.75 - 5.50
Molybdenum	2.80 - 3.30
Titanium	0.65 - 1.15
Aluminum	0.20 - 0.80
Cobalt	1.00 max.
Carbon	0.08 max.
Mangnaese	0.35 max.
Silicon	0.35 max.
Phosphorus	0.015 max.
Sulfur	0.015 max.
Boron	0.006 max.
Copper	0.30 max.

Table 1.3.1 – Limiting chemical composition, % of Inconel718 [25]

In order to accurately model Inconel 718, it was necessary to build a comprehensive table of temperature dependent properties (thermal conductivity, specific heat, density and latent heat behavior) as displayed in Table 1.3.2.

T (°C)	*k (W/m·K)*	*c (J/kg·K)*	*ρ (kg/m^{3})*
20	11.4	427.14	8,146
25	*11.5*	*428.05*	*8,144*
100	12.5	441.74	8,120
300	14.0	481.74	8,052
500	15.5	521.74	7,979
700	21.5	561.74	7,899
900	-	601.74	7,803
1,350	31.3	691.74	7,300
1,355	*31.4*	*692.74*	*7,294*
Latent Heat Behavior: 250,000 J/kg (1255° - 1337°C)			

Table 1.3.2 – Thermal conductivity (k), specific heat (C), density (ρ) of IN718 [25, 26, 27]

1.4 Microstructure of Inconel 718

Wrought Inconel 718 exhibits three equilibrium intermetallic precipitation phases: γ'(cubic order face-center), γ''(tetragonal body-centered) and δ (orthorhombic simple) shown in Figure 1.4.1 (a – c) [28, 29]. Figure 1.4.2(a) shows a micrograph of wrought Inconel 718 and Figure 1.4.2(b) is a magnified view of the dark sections. The plate-like structures are formations of the δ phase (columnar morphology), the very fine precipitates surrounding the δ phases are formations of the γ' and γ'' phases (equiaxed morphology), and the massive dark areas are the Laves phase [30, 31]. The Laves phase is only present in Inconel 718 that has solidified at a rate of less than 2°C per minute [32]. It has been found that the presence of Laves phase is a result of either non-equilibrium solidification or prolonged exposure to elevated temperatures, which directly relates to a slow solidification rate [33]. As such it is not typically observed in additive manufacturing.

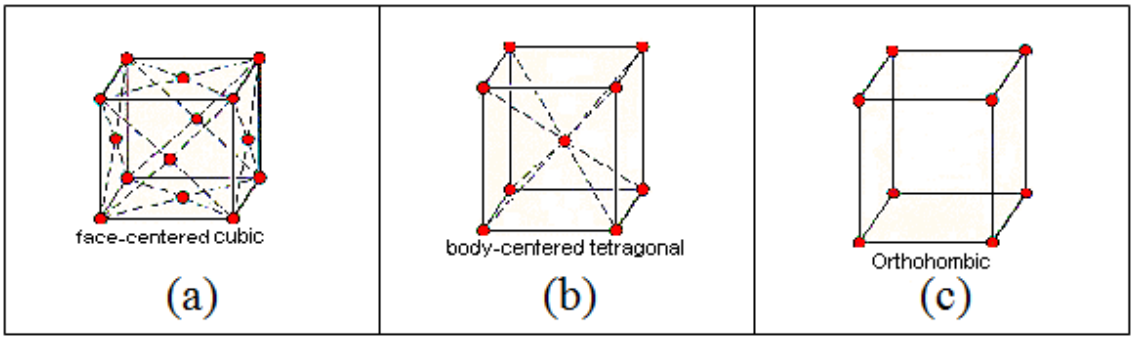

Figure 1.4.1 – Crystal structures of Inconel718: A. γ' phase face-centered cubic (FCC), B. γ'' body-centered tetragonal (BCT), C. δ orthorhombic structure [28] [29]

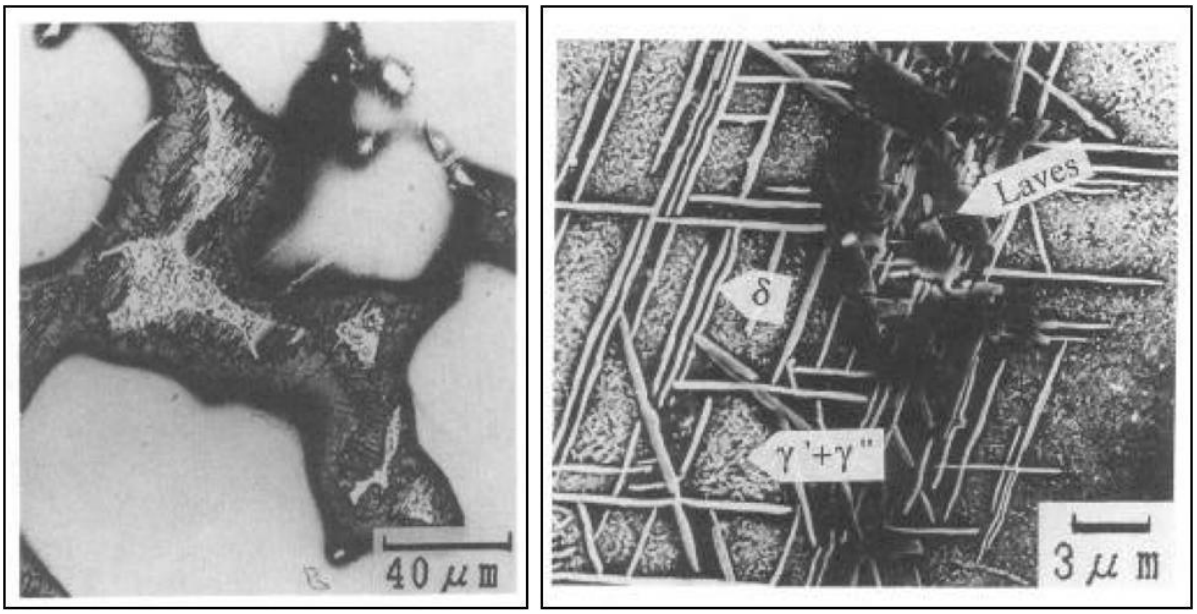

Figure 1.4.2 – Micrographs of wrought Inconel718: (a) 200x magnification, (b) 400x magnification of dark area of (a) [30]

It has been observed that IN718 solidification morphology is largely dependent on thermal gradient (*G*) and solidification rate (*R*), where a low G/R ratio results in a trend in microstructure toward equiaxed grains and a high G/R ratio produces a trend toward columnar grain structure [31].

1.5 Approach

The goal of this work is the development of process maps linking solidification microstructure to melt pool geometry in beam-based additive manufacturing of Inconel 718. It was necessary to set up fully non-linear finite element analysis (FEA) Abaqus® model to observe the changes in melt pool geometry as both absorbed beam power and beam velocity were changed. It has been shown that melt pool geometry has been linked to solidification microstructure in comparable alloys [6, 20, 19]. Once models for melt

pool geometry were successfully developed, efforts were made to seek solidification maps for Inconel 718. After discovering a solidification map, thermal gradient verses solidification rate simulations in ProCAST® casting software with cellular automaton-finite element (CAFE) were used to verify morphology results. The results of the non-linear FEA and the CAFE models were combined to produce the first microstructure process map in power verses velocity space for beam based additive manufacturing of Inconel 718.

1.6 Overview & Contributions

Overview

This thesis consists of 5 chapters. Chapter 2 explains the background that is rooted in understanding both the 2D and 3D Rosenthal solutions. It also highlights the importance of both thermal process and solidification maps as they pertain to additive manufacturing. The chapter finishes with the method used to incorporate FEA into additive manufacturing modeling.

Chapter 3 showcases the solidification map in thermal gradient verses solidification rate space for IN718, along with the method used to verify those results.

Chapter 4 expands on the FEA method and how the Rosenthal solution was used to guide the non-linear analysis for IN718. It finishes with the result of combining the CAFE and non-linear FEA results in the form of a microstructural process map with morphology regions in power verses velocity space for IN718. The final chapter includes conclusions from the results and suggestions for future work. The appendices include MATLAB® scripts, Abaqus® input decks for FEA and MATLAB® scripts used to extract data from the FEA simulations.

Contributions

The contributions of this thesis include the following:

1. Expanded existing methods in place for Ti-6Al-4V to other alloy system as it pertains to additive manufacturing solidification microstructure.
2. Validate previously published solidification microstructure maps in G vs. R space for IN718 using CAFE simulations.
3. Used 3D non-linear FEA guided by the 3D Rosenthal solution to produce a previously unpublished PV process map for solidification microstructure in beam-based additive manufacturing of IN718.

Chapter 2. Background

2.1 2D Rosenthal Solution

Daniel Rosenthal first introduced a moving point heat source solution to the welding community in 1946 [34]. The Rosenthal solution allowed for closed form calculations to determine melt pool geometry. Following work at Sandia [12, 13], this solution method was later used by Vasinonta et al. [35] to provide a quasi-steady-state solution during additive manufacturing of the thin-wall geometry shown in Figure 2.1.1, where the thickness b is assumed to be much smaller than the length L and height h. In Figure 2.1.1 V is the velocity of the moving heat source and αQ is the absorbed power of the heat source.

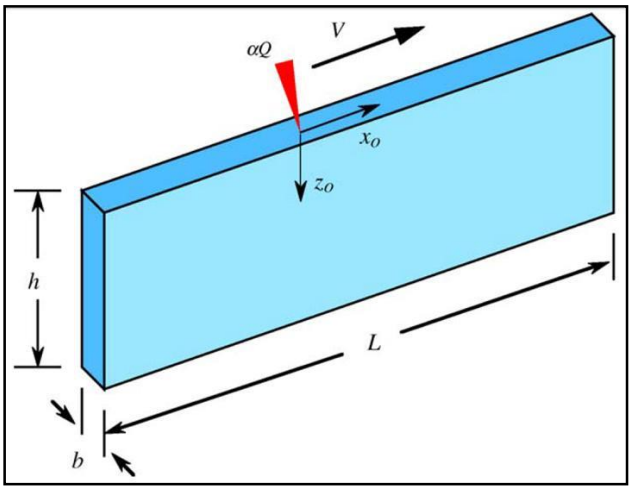

Figure 2.1.1- Thin-wall geometry considered [36]

Vasinotha et al. [36] was able to express the Rosenthal solution in a dimensionless form as

$$\bar{T} = e^{-\bar{x}_0} K_0 \sqrt{\bar{x}_0{}^2 + z_0{}^2}, \qquad \text{Eq. 2.1.1}$$

where K_0 was a zero order, modified Bessel function of the second kind. The spatial variables

$$\bar{x}_0 = \frac{x_0}{2k/\rho cV}, \bar{z}_0 = \frac{z_0}{2k/\rho cV}, \quad \text{Eq. 2.1.2}$$

are defined in terms of terms of current location (x_0,z_0), thermal conductivity (k), density (ρ), specific heat (c) and beam velocity (V). To convert the dimensionless temperature $\bar{T}$ to actual temperature,

$$\bar{T} = \frac{T-T_0}{\alpha Q/\pi kb}, \quad \text{Eq. 2.1.3}$$

was used where T_0 was the initial temperature of the wall.

For the Rosenthal solution, the thermophysical properties were assumed to be temperature-independent [36], whereas the reality is that thermal conductivity, density and specific heat are all temperature-dependent.

The thermal conditions that have been linked to solidification microstructure are cooling rate and thermal gradient [11, 2, 15]. The cooling rate was obtained by Bontha et al. [2] differentiating Eq. 2.1.1 with respect to dimensionless time $\bar{t}$, resulting in

$$\frac{\partial \bar{T}}{\partial \bar{t}} = e^{-(\bar{x}-\bar{t})}\left\{\frac{(\bar{x}-\bar{t})}{\sqrt{(\bar{x}-\bar{t})^2+\bar{z}_0{}^2}} K_1\left(\sqrt{(\bar{x}-\bar{t})^2+\bar{z}_0{}^2}\right) + K_0\left(\sqrt{(\bar{x}-\bar{t})^2+\bar{z}_0{}^2}\right)\right\}, \quad \text{Eq. 2.1.4}$$

The dimensionless coordinate $\bar{x}$ is related to the beams relative coordinate $\bar{x}_0$ by

$$\bar{x} = \bar{x}_0 + \bar{t}, \quad \text{Eq. 2.1.5}$$

where

$$\bar{t} = \frac{t}{2k/\rho cV^2}. \qquad \text{Eq. 2.1.6}$$

In Eq. 2.1.4, K_1 is the first order, modified Bessel function of the second kind. The dimensionless thermal gradient was obtained by differentiating Eq. 2.1.1 with respect to its spatial variables $\bar{x}_0$and $\bar{z}_0$ [6, 36] as

$$|\overline{\nabla T}| = \sqrt{\left(\frac{\partial \bar{T}}{\partial \bar{x}_0}\right)^2 + \left(\frac{\partial \bar{T}}{\partial \bar{z}_0}\right)^2}, \qquad \text{Eq. 2.1.7}$$

where

$$\frac{\partial \bar{T}}{\partial \bar{x}_0} = e^{-\bar{x}_0}\left\{\frac{\bar{x}_0}{\sqrt{\bar{x}_0{}^2 + \bar{z}_0{}^2}} K_1\left(\sqrt{\bar{x}_0{}^2 + \bar{z}_0{}^2}\right) + K_0\left(\sqrt{\bar{x}_0{}^2 + \bar{z}_0{}^2}\right)\right\} \qquad \text{Eq. 2.1.8}$$

and

$$\frac{\partial \bar{T}}{\partial \bar{z}_0} = e^{-\bar{x}_0}\left\{\frac{\bar{z}_0}{\sqrt{\bar{x}_0{}^2 + \bar{z}_0{}^2}} K_1\left(\sqrt{\bar{x}_0{}^2 + \bar{z}_0{}^2}\right)\right\}. \qquad \text{Eq. 2.1.9}$$

The dimensionless cooling rate $\partial \bar{T}/\partial \bar{t}$ and thermal gradient $|\overline{\nabla T}|$ can be related to actual cooling rate $\partial T/\partial t$ and thermal gradient$|\nabla \mathrm{T}|$ as,

$$\frac{\partial \bar{T}}{\partial \bar{t}} = \left(\frac{2\pi k^2 b}{\alpha Q \rho c V^2}\right)\frac{\partial T}{\partial t} \qquad \text{Eq. 2.1.10}$$

and

$$|\overline{\nabla T}| = \left(\frac{2\pi k^2 b}{\alpha Q \rho c V}\right)|\nabla T|. \qquad \text{Eq. 2.1.11}$$

2.2 3D Rosenthal Solution

Similar to the 2D Rosenthal solution, the 3D Rosenthal solution provided a quasi-steady-state solution to the 3D heat conduction equation and is applicable to bulky 3D geometries as shown in Figure 2.2.1 [34].

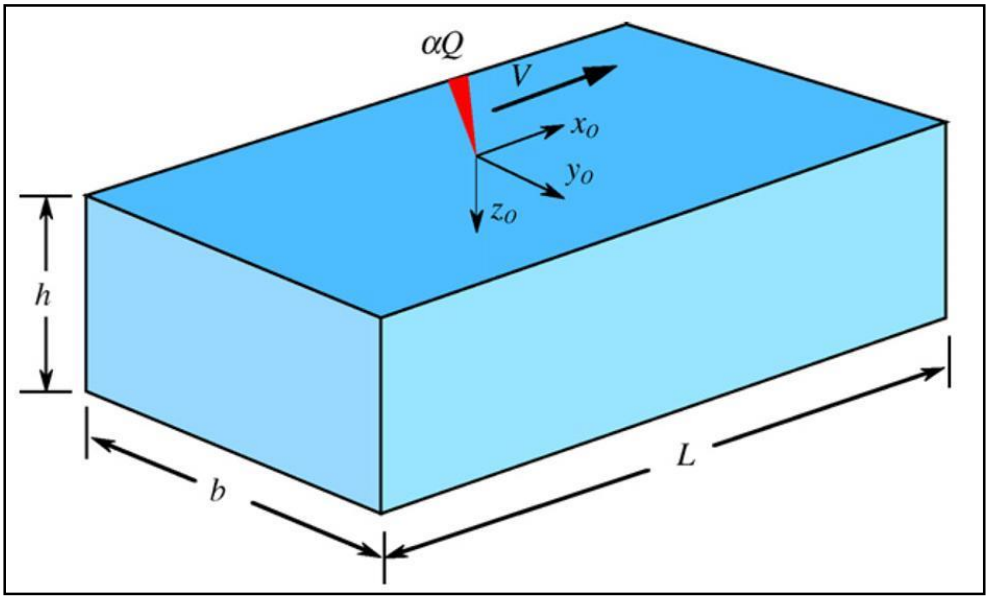

Figure 2.2.1 – Bulky 3D geometry considered [36]

The Rosenthal point source solution assumes the substrate geometry where the height *h*, base *b* and length *L* are all infinitely large when compared to the melt pool. The three-dimensional flow of heat in an infinite space was expressed in dimensionless form by Vasinonta et al. [35] as

$$\bar{T} = \frac{e^{-\left(\bar{x}_0+\sqrt{\bar{x}_0{}^2+\bar{y}_0{}^2+\bar{z}_0{}^2}\right)}}{2\sqrt{\bar{x}_0{}^2+\bar{y}_0{}^2+\bar{z}_0{}^2}}, \qquad \text{Eq. 2.2.1}$$

where

$$\bar{T} = \frac{T-T_0}{(\alpha Q/\pi k)(\rho c V/2k)}, \qquad \text{Eq. 2.2.2}$$

and

$$\bar{x}_0 = \frac{x_0}{2k/\rho cV}, \bar{y}_0 = \frac{y_0}{2k/\rho cV} \text{ and } \bar{z}_0 = \frac{z_0}{2k/\rho cV}. \quad \text{Eq. 2.2.3}$$

In Eq. 2.2.1, the normalized temperature $\bar{T}$ is defined by the dimensionless spacial variables, $\bar{x}_0, \bar{y}_0$ and $\bar{z}_0$ [35]. As in the 2D solution, the parameters of interest in controlling solidification microstructure are cooling rate and thermal gradient, which were obtained by Bontha et al. [2, 11] through differentiation of Eq. 2.2.1 with respect to the normalized time as

$$\frac{\partial \bar{T}}{\partial \bar{t}} = \frac{1}{2} \frac{e^{-\left((\bar{x}-\bar{t})+\sqrt{(\bar{x}-\bar{t})^2+{\bar{y}_0}^2+{\bar{z}_0}^2}\right)}}{\sqrt{(\bar{x}-\bar{t})^2+{\bar{y}_0}^2+{\bar{z}_0}^2}} \left\{1 + \frac{(\bar{x}-\bar{t})}{\sqrt{(\bar{x}-\bar{t})^2+{\bar{y}_0}^2+{\bar{z}_0}^2}} + \frac{(\bar{x}-\bar{t})}{\left((\bar{x}-\bar{t})^2+{\bar{y}_0}^2+{\bar{z}_0}^2\right)}\right\}. \quad \text{Eq. 2.2.4}$$

Similarly the dimensionless thermal gradient was obtained by differentiating Eq. 2.2.1 with respect to the dimensionless spatial coordinates $\bar{x}_0, \bar{y}_0$ and $\bar{z}_0$ as

$$|\overline{\nabla T}| = \sqrt{\left(\frac{\partial \bar{T}}{\partial \bar{x}_0}\right)^2 + \left(\frac{\partial \bar{T}}{\partial \bar{y}_0}\right)^2 + \left(\frac{\partial \bar{T}}{\partial \bar{z}_0}\right)^2}, \quad \text{Eq. 2.2.5}$$

where

$$\frac{\partial \bar{T}}{\partial \bar{x}_0} = -\frac{1}{2} \frac{e^{-\left(\bar{x}_0+\sqrt{{\bar{x}_0}^2+{\bar{y}_0}^2+{\bar{z}_0}^2}\right)}}{\sqrt{{\bar{x}_0}^2+{\bar{y}_0}^2+{\bar{z}_0}^2}} \left\{1 + \frac{\bar{x}_0}{\sqrt{{\bar{x}_0}^2+{\bar{y}_0}^2+{\bar{z}_0}^2}} + \frac{\bar{x}_0}{\left({\bar{x}_0}^2+{\bar{y}_0}^2+{\bar{z}_0}^2\right)}\right\}, \quad \text{Eq. 2.2.6}$$

$$\frac{\partial \bar{T}}{\partial \bar{y}_0} = -\frac{1}{2} \frac{\bar{y}_0 e^{-\left(\bar{x}_0+\sqrt{{\bar{x}_0}^2+{\bar{y}_0}^2+{\bar{z}_0}^2}\right)}}{\left({\bar{x}_0}^2+{\bar{y}_0}^2+{\bar{z}_0}^2\right)} \left\{1 + \frac{1}{\sqrt{{\bar{x}_0}^2+{\bar{y}_0}^2+{\bar{z}_0}^2}}\right\}, \quad \text{Eq. 2.2.7}$$

and

$$\frac{\partial \bar{T}}{\partial \bar{z}_0} = -\frac{1}{2}\frac{\bar{z}_0 e^{-\left(\bar{x}_0+\sqrt{\bar{x}_0{}^2+\bar{y}_0{}^2+\bar{z}_0{}^2}\right)}}{\left(\bar{x}_0{}^2+\bar{y}_0{}^2+\bar{z}_0{}^2\right)}\left\{1+\frac{1}{\sqrt{\bar{x}_0{}^2+\bar{y}_0{}^2+\bar{z}_0{}^2}}\right\}. \quad \text{Eq. 2.2.8}$$

The dimensionless cooling rate $\partial \bar{T}/\,\partial \bar{t}$ and thermal gradient $|\overline{\nabla T}|$ can be related to actual cooling rate $\partial T/\,\partial t$ and thermal gradient$|\nabla \mathrm{T}|$ as

$$\frac{\partial \bar{T}}{\partial \bar{t}} = \left(\frac{2k}{\rho c V}\right)^2 \left(\frac{\pi k}{\alpha Q V}\right)\frac{\partial T}{\partial t}, \quad \text{Eq. 2.2.9}$$

and

$$|\overline{\nabla T}| = \left(\frac{2k}{\rho c V}\right)^2 \left(\frac{\pi k}{\alpha Q}\right)|\nabla T|. \quad \text{Eq. 2.2.10}$$

2.3 Thermal Process Maps

The Rosenthal solution not only gave the ability to define dimensionless variables but enabled researchers to develop process maps for solidification cooling rate and thermal gradient [2, 11, 15]. The development of these process maps by Bontha et al. provided significant insight into the effects of changes in process variables and size-scale on trends in solidification microstructure. Values of both dimensionless cooling rate and thermal gradient at the start of solidification were found by evaluating Eq. 2.1.4 and Eq. 2.1.7 for the 2D case, or Eq. 2.2.4 and Eq. 2.2.5 for the 3D case, along the melt pool (solidification) boundary in the (x_0, z_0) plane. The coordinates (x_0, z_0) that lie on the melt pool boundary were found by replacing T in Eq. 2.1.1 or Eq. 2.2.1with the alloy's melting temperature T_m. A numerical root finding scheme was then used to find the locations of the melt pool boundary. The resulting 2D process maps for solidification cooling rates and thermal gradients as a function of normalized melting temperature $\bar{T}_m$ and relative depth within the melt pool $\bar{z}_0/\bar{z}_m$ were plotted. These results can are shown in Figure 2.3.1 and Figure 2.3.2, along with 3D process maps in Figure 2.3.3 and Figure

2.3.4. Normalized depth varied in the range $0 \leq \bar{z}_0/\bar{z}_m \leq 1$, where $\bar{z}_m$ indicated the deepest extent of the melt pool for a given $\bar{T}_m$ value.

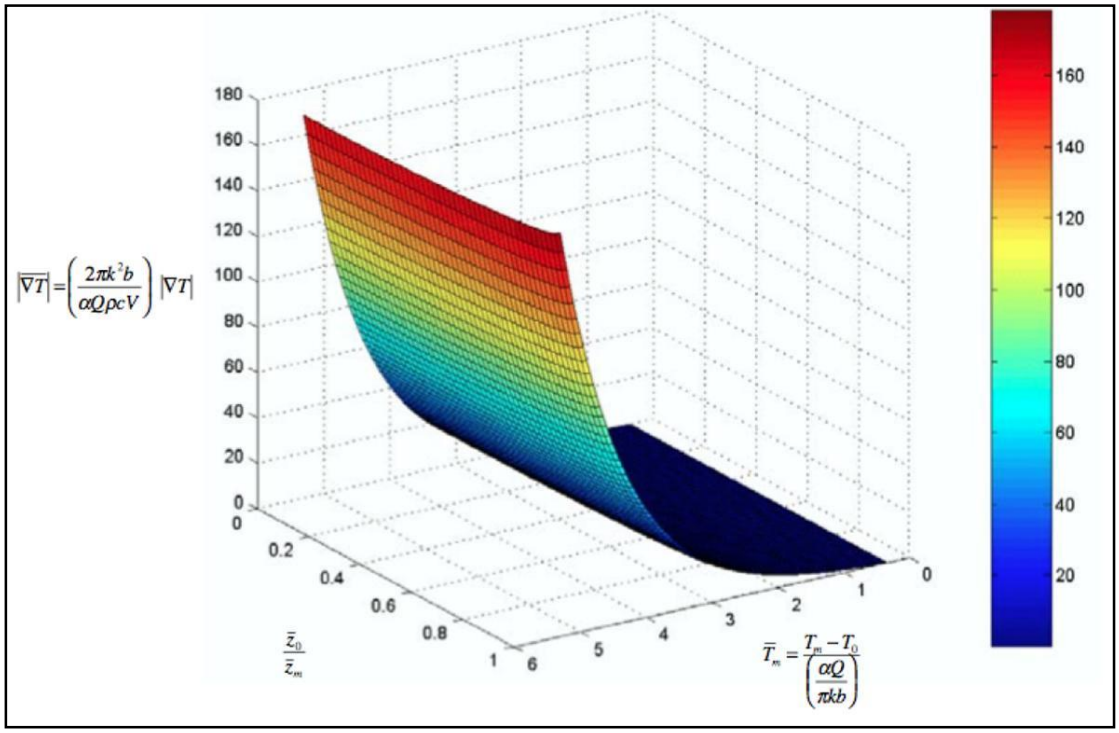

Figure 2.3.1 – 2D Rosenthal solution thermal gradient $|\overline{\nabla T}|$ process map [2, 11, 15]

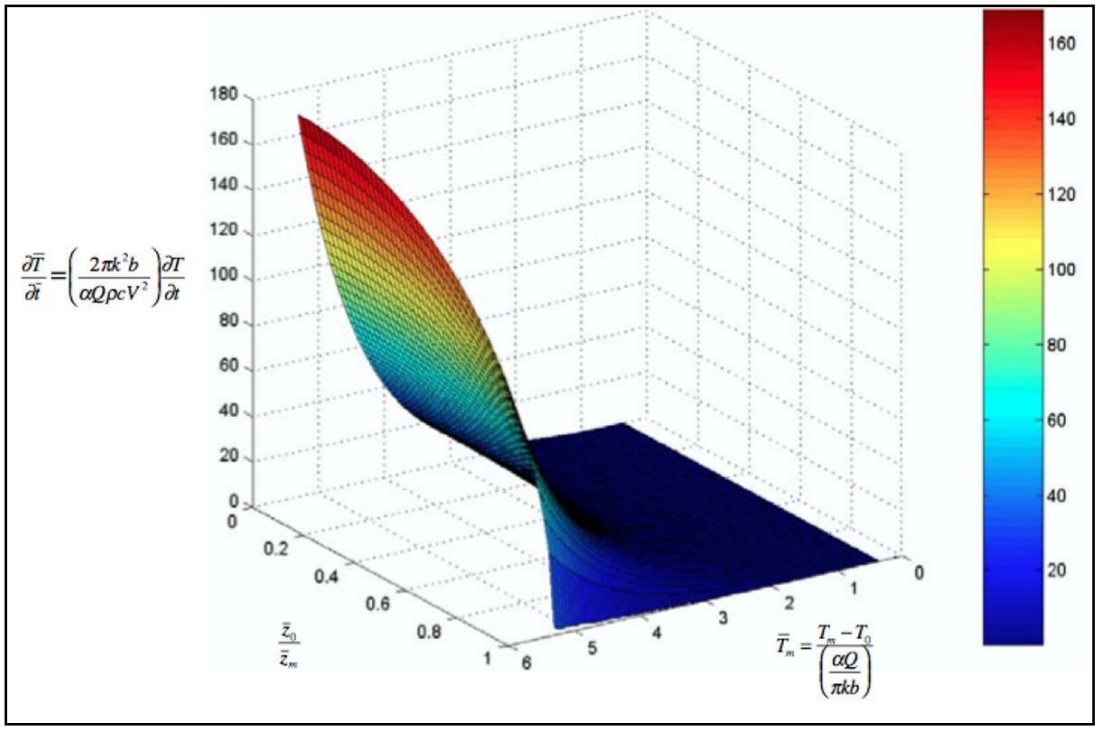

Figure 2.3.2 – 2D Rosenthal solution cooling rate $\partial T / \partial t$ process map [2, 11, 15]

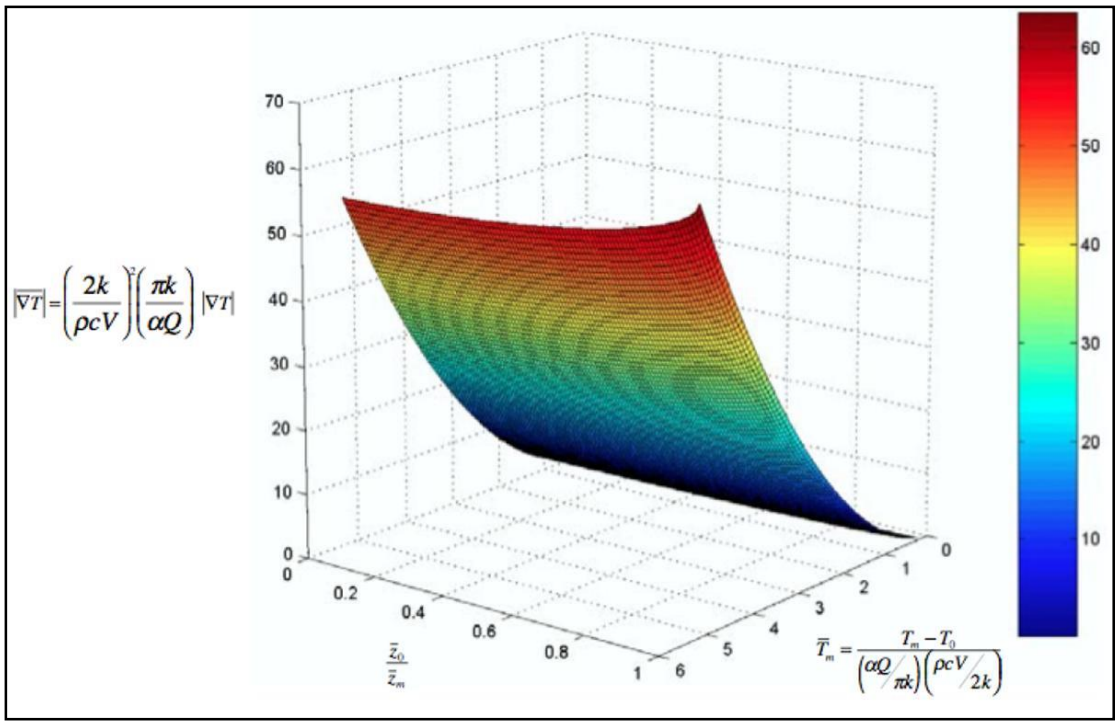

Figure 2.3.3 – 3D Rosenthal solution thermal gradient $|\overline{\nabla T}|$ process map [2, 11, 15]

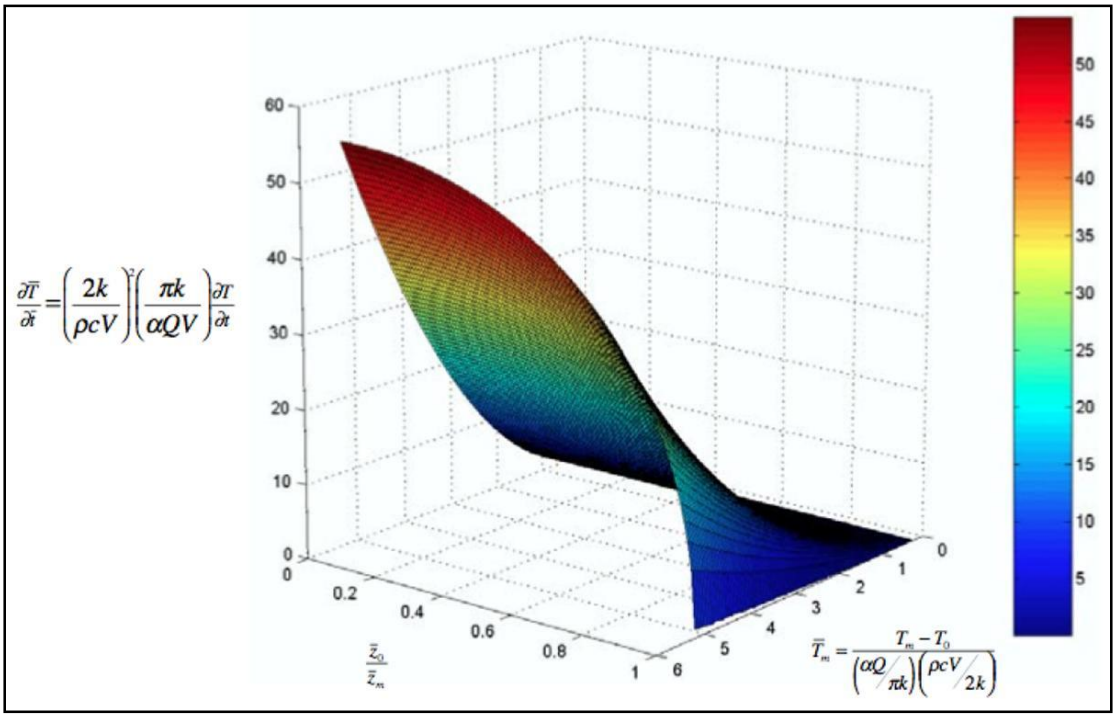

Figure 2.3.4 – 3D Rosenthal solution cooling rate $\partial T / \partial t$ process map [2, 11, 15]

Figure 2.3.3 shows the thermal gradient stays fairly consistent throughout the melt pool depth, similar to Figure 2.3.1, the 2D process map; however, both the 2D and 3D maps indicates that the thermal gradient is very sensitive to the melting temperature [2, 6, 19]. Both the 2D and 3D process maps of cooling rate, illustrate a major variance through the depth of the melt pool with maximums and minimums at $\bar{z}_0/\bar{z}_m = 0$ and $\bar{z}_0/\bar{z}_m = 1$ [11, 15]. The 3D cooling rate is a bit more sensitive to melt temperature than that of the 2D cooling rate.

2.4 Incorporation of Finite Element Analysis (FEA)

As previously stated, the Rosenthal solution provided the means for vast amounts of numerical data collection, largely due to the ability to calculate and manipulate the equations very quickly. Recall that the basis of the Rosenthal solution was that temperature dependent properties were assumed to be constant, whereas in reality they

are not. Following the work of Vasinonta et al., Bontha et al. developed a fully non-linear finite element analysis to simulate a 3D beam-based additive manufacturing process that varied in process space [11, 35]. The model shown in Figure 2.4.1, was a half-symmetric model of a bulky 3D geometry that used 8-node bilinear thermal elements generated using the commercial software package ABAQUS®. The model approximated the laser as a moving point heat source beginning at the left side of Figure 2.4.1 and mainly along the top surface at time intervals the corresponding to a constant beam velocity.

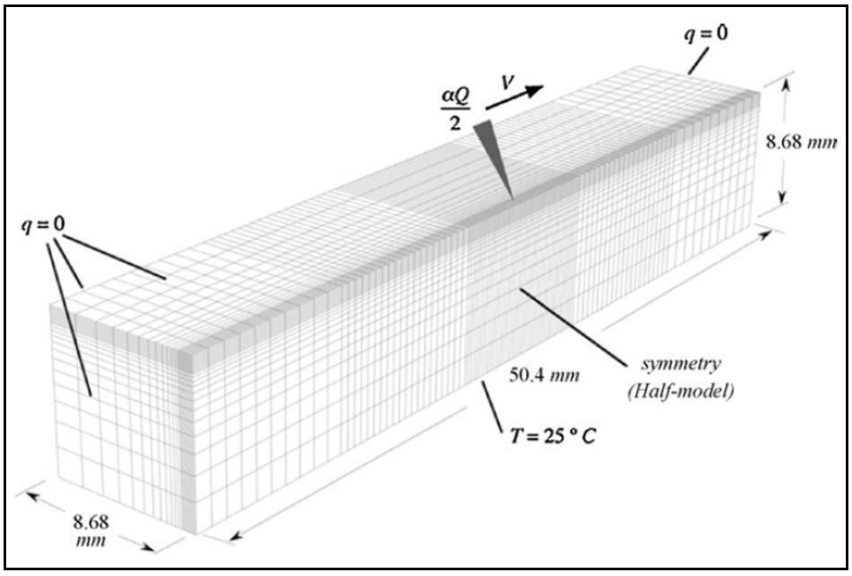

Figure 2.4.1 – Example of 3D non-linear FEA [11]

A comparison of results for non-linear FEA simulations and Rosenthal solutions was completed to determine the utility of the better. Figure 2.4.2 shows a comparison between varying beam powers as velocity was held as a constant in *G vs. R* space [11].

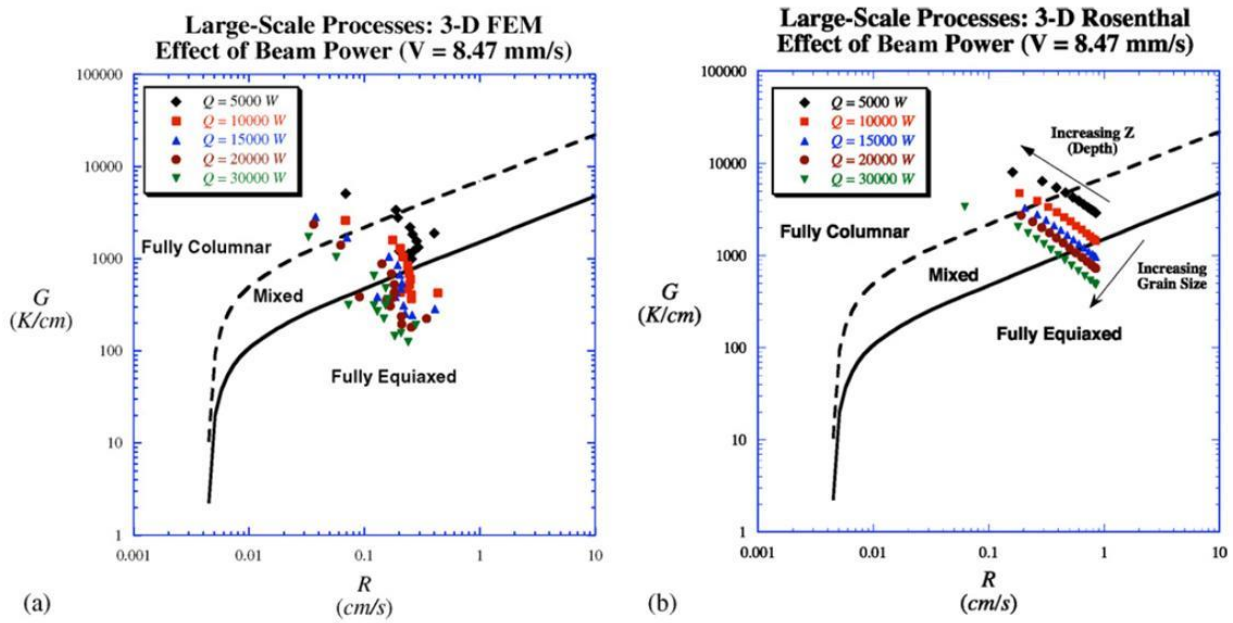

Figure 2.4.2 – Comparison of trends between nonlinear FEA and 3D Rosenthal solution [11]

The Rosenthal solution does not match the FEA (also referred to as finite element model (FEM)) results exactly; however, the Rosenthal solution can predict trends in solidification space reasonably well. This comparison gave future researchers the ability to achieve a first order approximation using the 3D Rosenthal solution to target specific melt pool geometries.

2.5 Solidification Maps for Ti-6Al-4V

Ti-6Al-4V is a two phase (α, β) alloy where prior β grains formed during solidification can have either equiaxed grain structure or a more columnar grain structure, as shown in Figure 2.5.1(a)(b). Coupled with the formation of α within and along the boundaries, the size and morphology of the β grains are linked to mechanical properties [19].

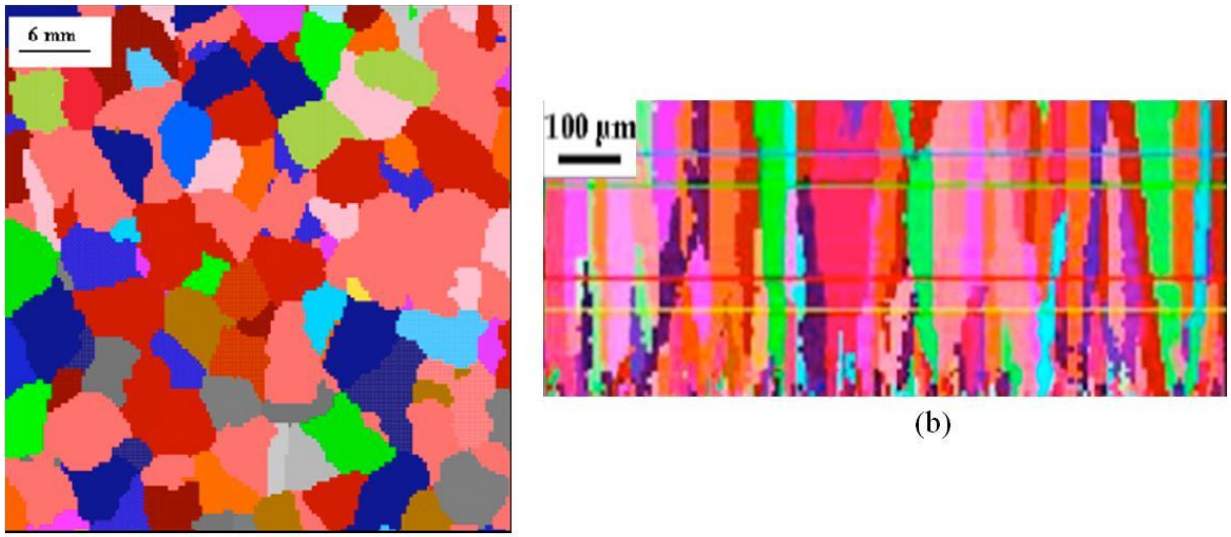

(a) (b)

Figure 2.5.1 – Simulated grain growth: Fully equiaxed grains (a) – Fully columnar grains (b) [6, 16]

As discussed by Kobryn et al. [18], morphology regions can be mapped out in thermal gradient *G* as a function of solidification rate *R* space, where $G = |\nabla T|$ and

$$R = \frac{1}{G}\frac{\partial T}{\partial t}. \qquad \text{Eq. 2.5.1}$$

Kobryn et al. calibrated solidification microstructure regions experimentally and define these regions as fully equiaxed, fully columnar or mixed morphology in G vs R space [17, 18].

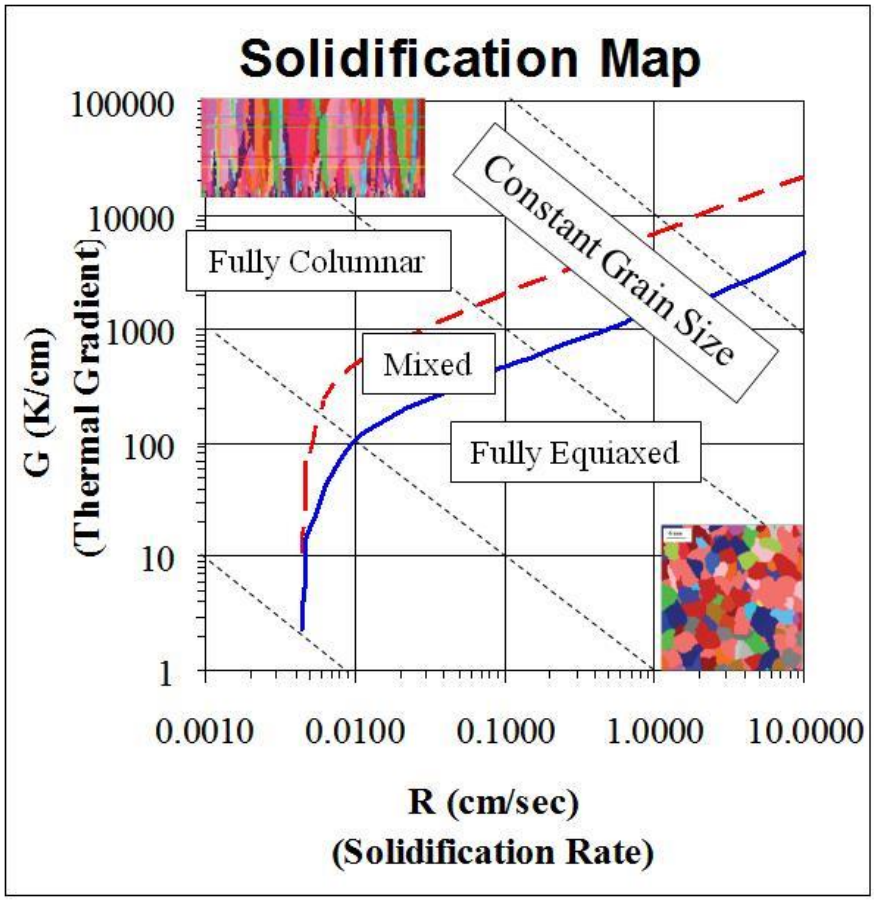

Figure 2.5.2 – Solidification map of Ti-6Al-4V in G vs. R space [6, 17, 18]

Figure 2.5.2 shows the different morphology regions along with examples of fully equiaxed and fully columnar grain structures, where a mixed morphology would simply be a combination of the two. It was observed that surface morphology tended to be equiaxed as the solidifications were normally higher. Also in Figure 2.5.2, diagonal lines represent lines of constant grain size [6]. Gockel et al. [37] (formerly Davis) has linked solidification maps to process maps, showing absorbed power vs. velocity with lines of constant melt pool area are the same lines of constant grain size, thus linking solidification microstructure to melt pool geometry. Being able to map out microstructure morphology regions in *P vs. V* space allows for controlling solidification microstructure.

By simply consulting a map of the microstructure and using Figure 2.5.3, one can make the necessary adjustments to beam power or velocity to create a specific microstructure.

The process map for Ti-6Al-4V with morphology regions shown in Figure 2.5.3, illustrates lines of constant grain size, which Davis related to lines of constant melt pool area, as the dashed green purple and cyan lines. It also gives the grain morphology boundaries, designated by the red dashed and solid blue lines. This shows an increase in power relates to a fully equiaxed morphology for Ti-6Al-4V and was the first P-V process map linking microstructure to melt pool geometry and corresponding additive manufacturing design parameters, as in Figure 2.5.4 [37].

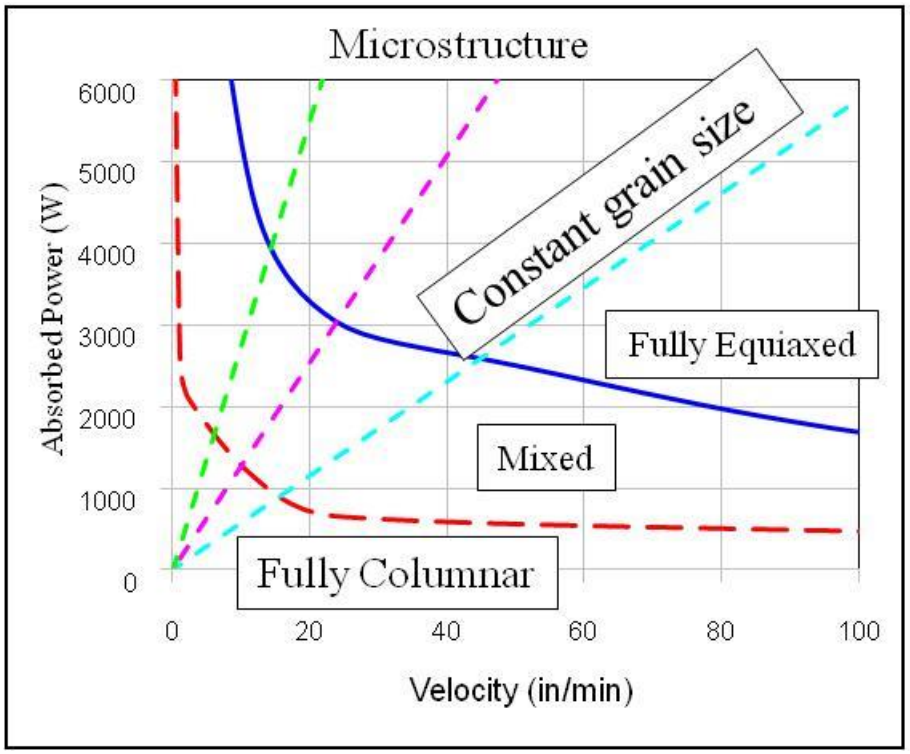

Figure 2.5.3 – Microstructure map of Ti-6Al-4V in P vs. V space [37]

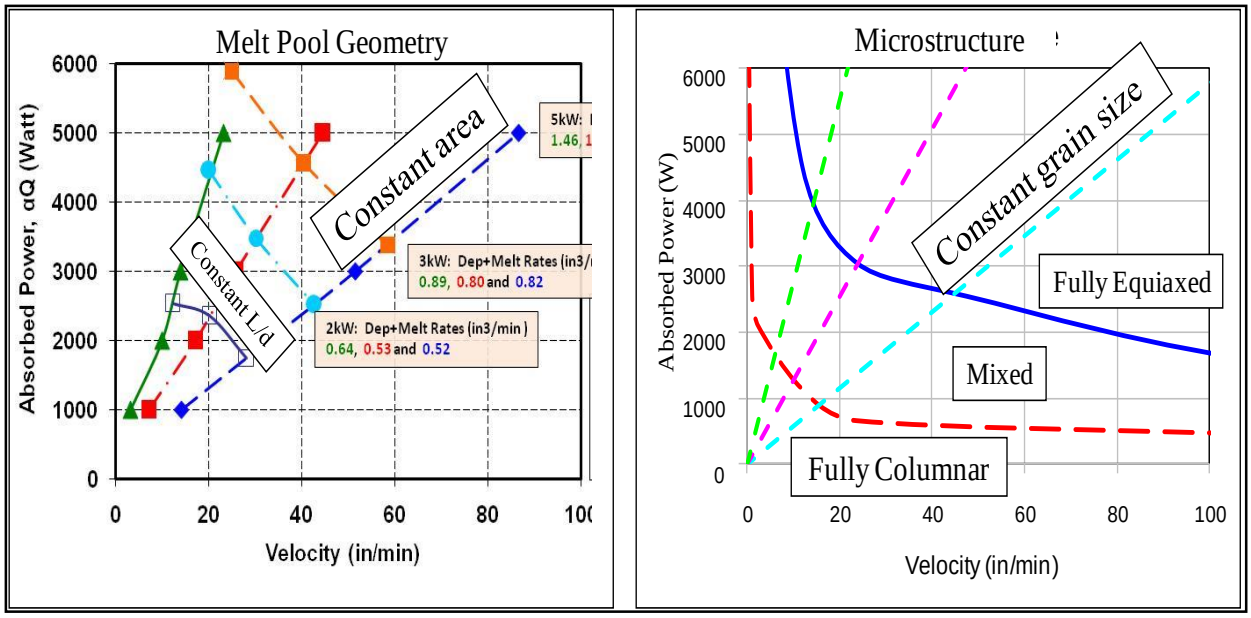

Figure 2.5.4 – Link between melt pool geometry and microstructure for Ti-6Al-4V [37]

Chapter 3. Inconel 718® Microstructure Analysis

3.1 Solidification Map Inconel 718®

Nastiac, et. al. did extensive experimental and analytical research in the area of material characterization for Inconel 718 that resulted in the solidification map for IN718 shown in Figure 3.1.1 [24]. This is similar to solidification maps used by previous authors for parallel work in Ti-6Al-4V [2, 6, 18, 19], shown in Figure 2.5.2. When comparing the solidification maps of IN718 and Ti-6Al-4V, as shown in Figure 3.1.2, it can be seen that changing the alloy causes the morphology regions to shift in both directions of *G vs. R* space.

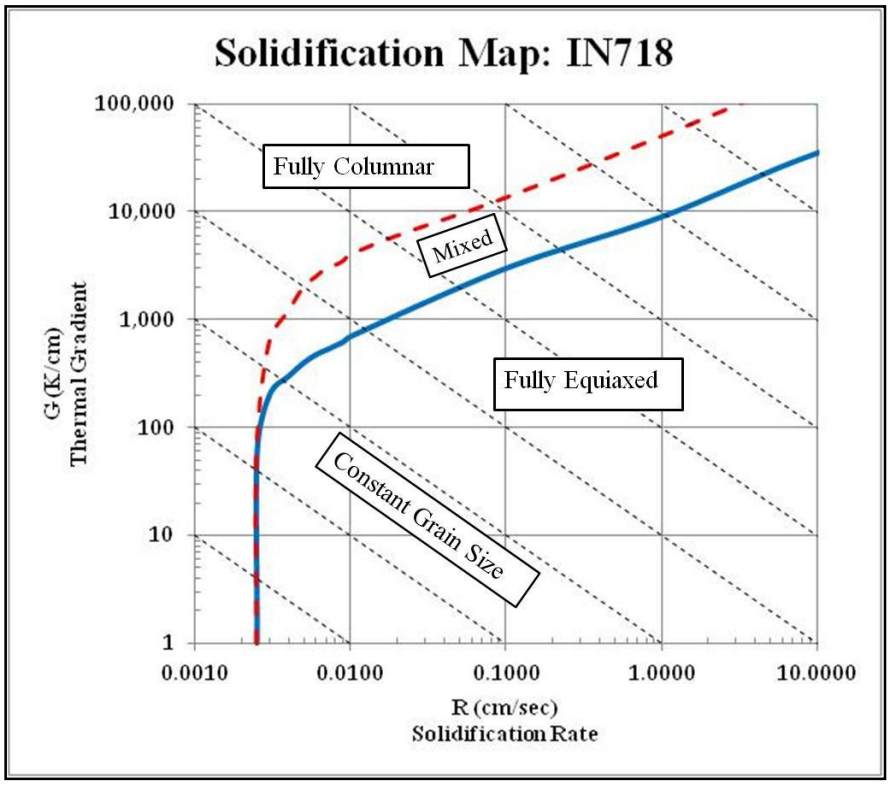

Figure 3.1.1 – Solidification map of IN718 [24]

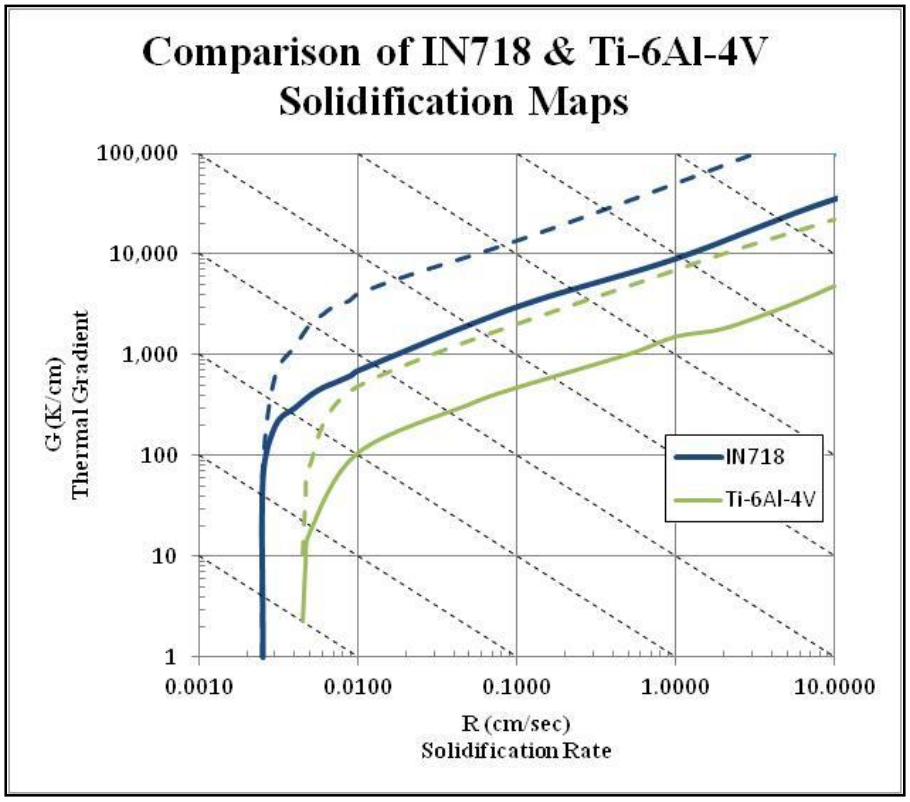

Figure 3.1.2 – Comparison of solidification maps, IN718 & Ti-6Al-4V

3.2 ProCAST® Modeling to Verify Accuracy of Solidification Map

Over the last 20 years ESI® has developed ProCAST®, an advanced tool geared toward simulations for improving castings in the foundry industry. ProCAST® is based on finite element technology and is capable of predicting deformations and residual stresses. It is capable of modeling processes like semi-solid modeling, core blowing, centrifugal casting, lost foam and continuous casting [38]. Within the ProCAST® software a cellular automation-finite element (CAFE) module is available, that calculates and simulates grain nucleation and growth. The software was used to simulate ingot castings which verified that the solidification map used was accurate in predicting grain morphology.

The first step in creating a ProCAST® model was to design a casting. Previous work with Ti-6Al-4V used a simple casting that was gravity fed into a sand casting as shown in Figure 3.2.1, with the parameters shown in Table 3.2.1 [16].

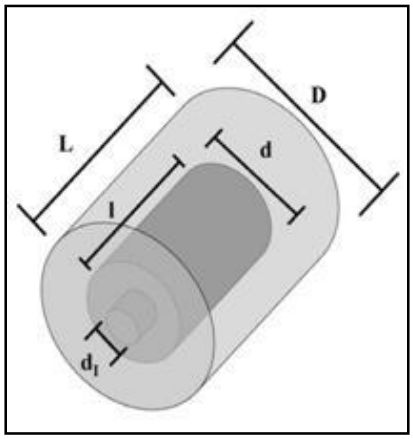

Figure 3.2.1 – Simple casting design for ProCAST® simulation [16]

Ingot #	Casting Dimenions (in)				
	d	*D*	*l*	*L*	d_1
1	*1*	*3*	*7.5*	*9*	*2*
2	*2.5*	*5.5*	*9*	*10.5*	*2*
3	*5*	*7.25*	*14.5*	*18.5*	*2*

Table 3.2.1 – Previous casting parameters [16]

In prior work with Ti-6Al-4V, three separate sample sizes were used to alter the thermal gradient and solidification rate. For this work, ingot #2 parameters were used for the initial ProCAST® set up. The geometry of the ingot and filling sprue were created first as shown in Figure 3.2.2(a). Next, the mold was created as shown in Figure 3.2.2(b). Once the geometries were created they were mated together, as shown in Figure 3.2.3.

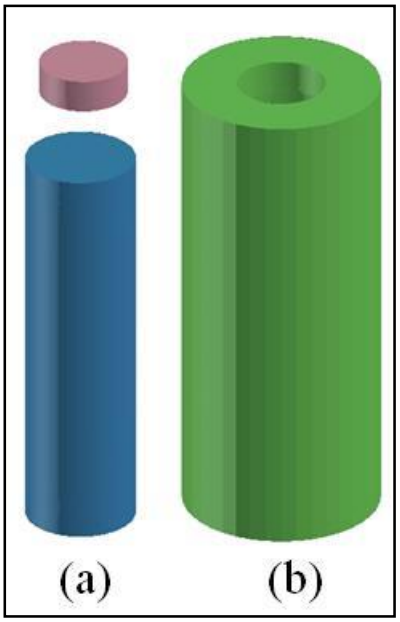

Figure 3.2.2 – ProCAST® simulation geometry

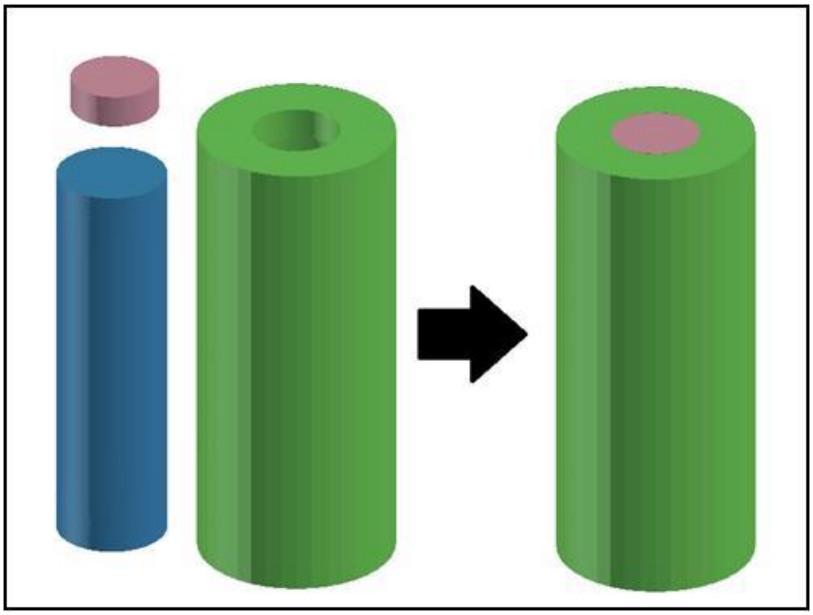

Figure 3.2.3 – Mating sprue, casting and mold geometries

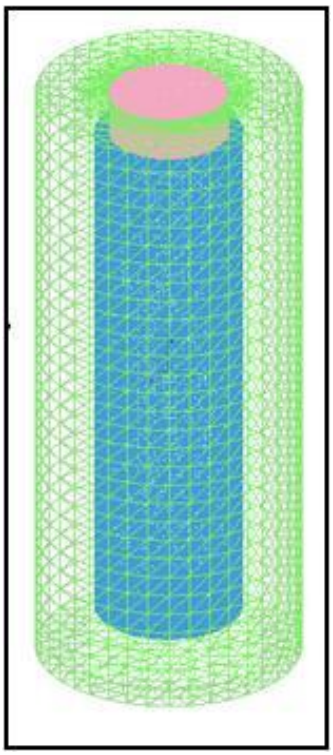

Figure 3.2.4 – Meshed ProCAST® model

After the model was mated and no discontinuity existed, the model was meshed as shown in Figure 3.2.4. Once the model was meshed the volumes were assigned. For these simulations, Inconel 718 was assigned to both the sprue and the ingot. Olivine sand was assigned to the mold, as it is a common cast material for this application [38]. Table 3.2.2 shows the casting parameters used for all simulations. With volumes defined, the process conditions were assigned. Process conditions control the heat flow interactions between the individual volumes as well as the effects of boundary conditions. The next step was to define simulation parameters, giving control of general thermal and flow parameters.

Name	*Type*	*Material*	*Fill %*	*Initial Temperature*	*Stress Type*
Ingot	Alloy	Inconel 718	100	1380.00 °C	Rigid
Mold	Mold	Olivine Sand	100	30.00 °C	Rigid
Sprue	Alloy	Inconel 718	100	1380.00 °C	Rigid

Table 3.2.2 – Casting Parameters

Prior to starting the simulation, a final data check was completed. This check ensured the volume assignments, process conditions and simulation parameters were not in conflict. After the simulation was completed, Visual Viewer® was the software package used for post-processing of the simulation. In addition, thermal history over the entire casting process time to solidification was noted for all these simulations. Figure 3.2.5 shows both a 3D and 2D slice view of the solidification time plot, with the time to solidification scale in seconds. Thermal gradients and solidification rates were manually extracted from the model in the post-processing step of the simulation.

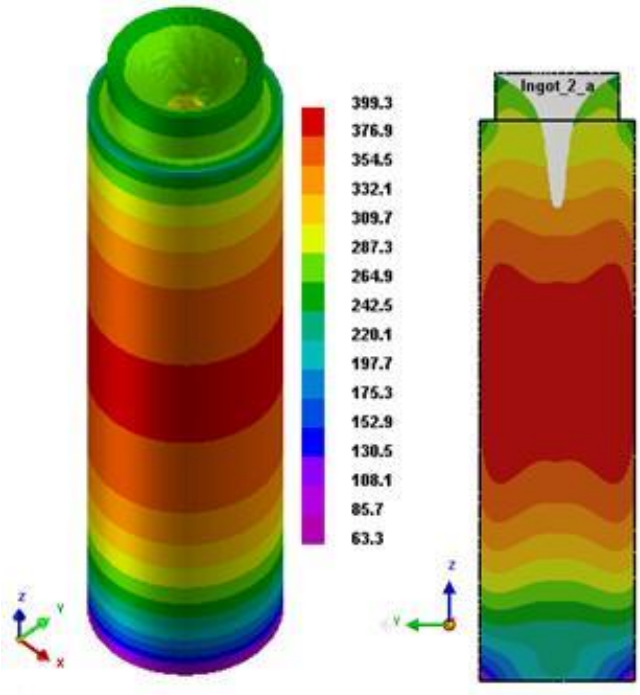

Figure 3.2.5 – 3D and 2D slice of ingot simulation solidification, scale in seconds

3.3 Cellular Automaton-Finite Element (CAFE) Implementation

Implementation of cellular automaton-finite element (CAFE) was needed to determine precipitate formation at specific thermal gradients and solidification rates. As previously noted, temperature information was extracted from ProCAST® in Visual Viewer, the post-processing package. If a microstructure growth simulation is required, the CAFE module must be initialized before the material selection step of the simulation setup. The CAFE simulation initiates grain nucleation and growth numerically and statistically. When defining the material the software pulls nucleation parameters from its alloy specific database. Once the grain growth parameters are calculated, the material must be saved in order to be used as an active assignable volume. The software calculates grain undercooling and generation randomization within its solver. The CAFE module performs calculations after the thermal data is recorded and plots upon request in Visual Viewer. Figure 3.3.1(a – d) shows the solidification progression of an ingot in ProCAST with CAFE, (a) 3D computer aided design, (b) finely meshed geometry, (c) temperature solutions verses time and (d) microstructure simulation. It was observed that the CAFE simulation increased the run time significantly, up to 600%. Figure 3.3.2 shows an example of a CAFE result in Visual Viewer where the scale shows mis-oriented grain boundaries, allowing visual confirmation of precipitate formations.

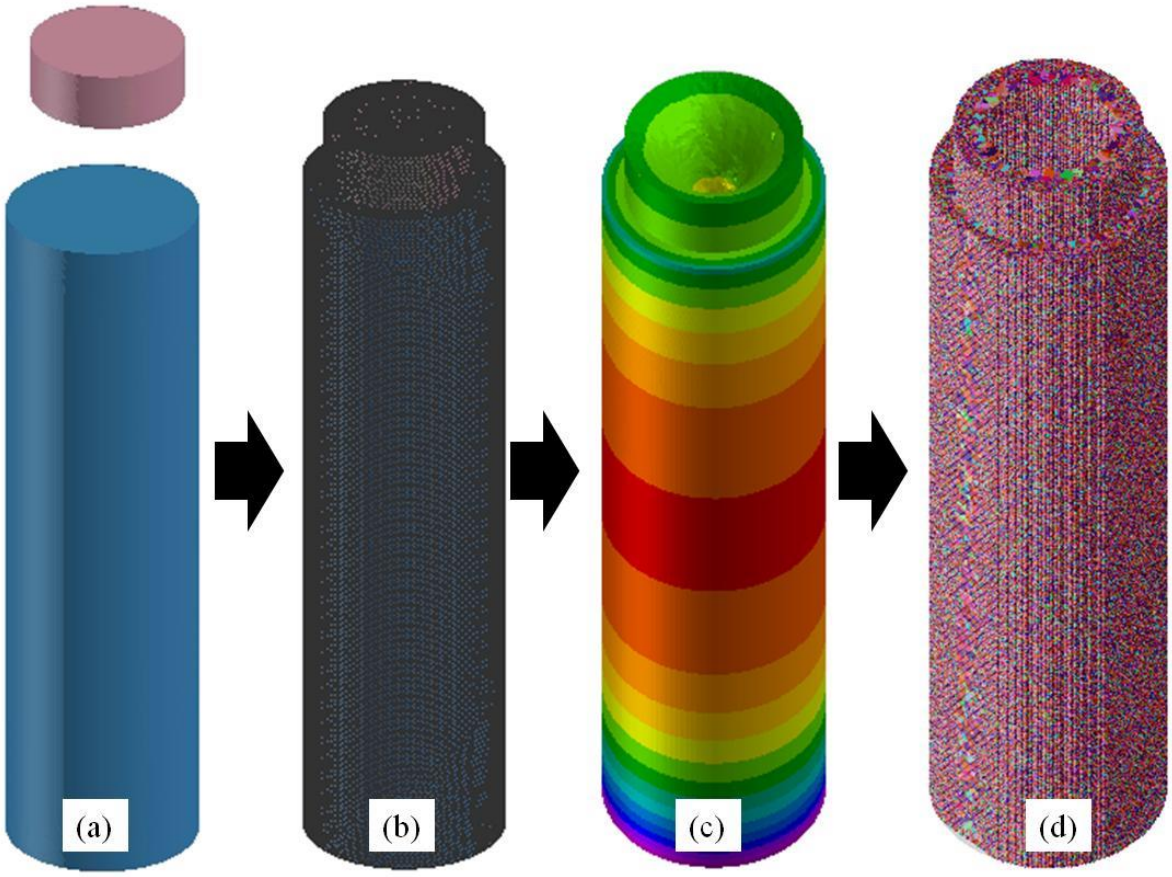

Figure 3.3.1 – Progression of ingot simulation resulting in microstructure simulation

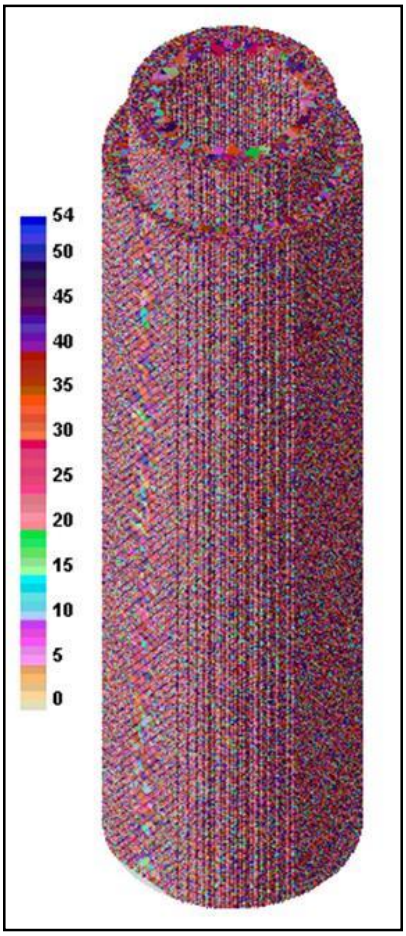

Figure 3.3.2 –CAFE simulation scale shows degrees mis-orientation of grain boundaries

3.4 Comparison of Experimental and Simulated Results

To ensure confidence in all of the setup parameters and viewable results produced with the ProCAST and CAFE software, ingots used in a 1999 JOM article were modeled and compared. The ingots that were modeled had a diameter of 500mm and were allowed to air cool. Figure 3.4.1(a) is an actual microstructure from a casting [39], whereas Figure 3.4.1(b) is simulated microstructure from a ProCAST and CAFE model of the same ingot. These were both sliced in the *x-y* plane from the middle of the ingot, showing largely columnar grains in the bulk of the ingot and a more equiaxed grain structure near the surface. Figure 3.4.2 shows the comparison between the surface microstructure in the

casted ingots (a) and simulated (b) microstructure. The surface had a very equiaxed grain structure, as it is subject to a much higher solidification rate than the center of the ingot. The similarities gave confidence in determining solidification microstructure in IN718.

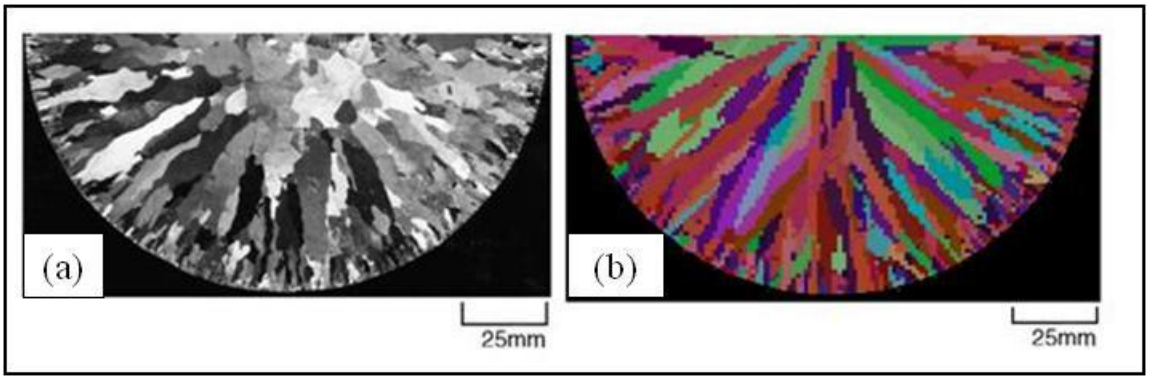

Figure 3.4.1 – Comparison between experimental IN718 ingot [39] and CAFE simulation microstructure, slice from center of ingot

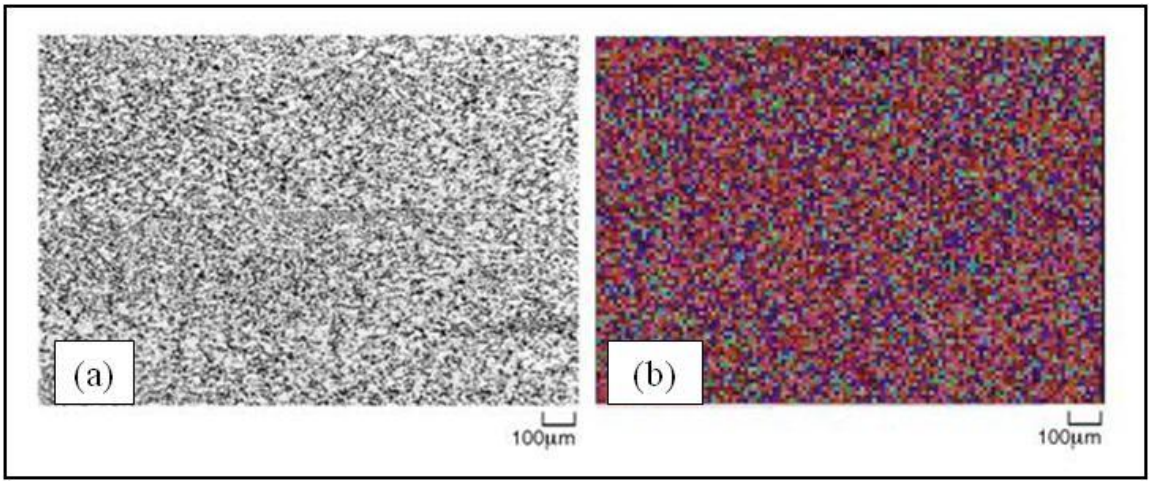

Figure 3.4.2 – Comparison between experimental IN718 ingot [39] and CAFE simulation microstructure, on the surface

3.5 Verify IN718 Solidification Map

Due to the scarceness of published IN718 solidification maps, the ProCAST with CAFE simulation was used to verify the morphology regions defined in Figure 3.1.1. Several simulations were accomplished, with varying cooling parameters to alter the thermal gradient and solidification rate. These changes altered the microstructure, as the map

indicated they would. An aspect ratio of 1 was used to categorize the equiaxed (γ' / γ'') precipitate formation . Figure 3.5.1 shows examples ***A*** and ***B*** of both fully columnar (δ) and equiaxed (γ' / γ'') precipitate formation, in the appropriate regions of the solidification map. This showed that the two regions were accurately defined on this solidification map [24] and would be suitable for use in this work.

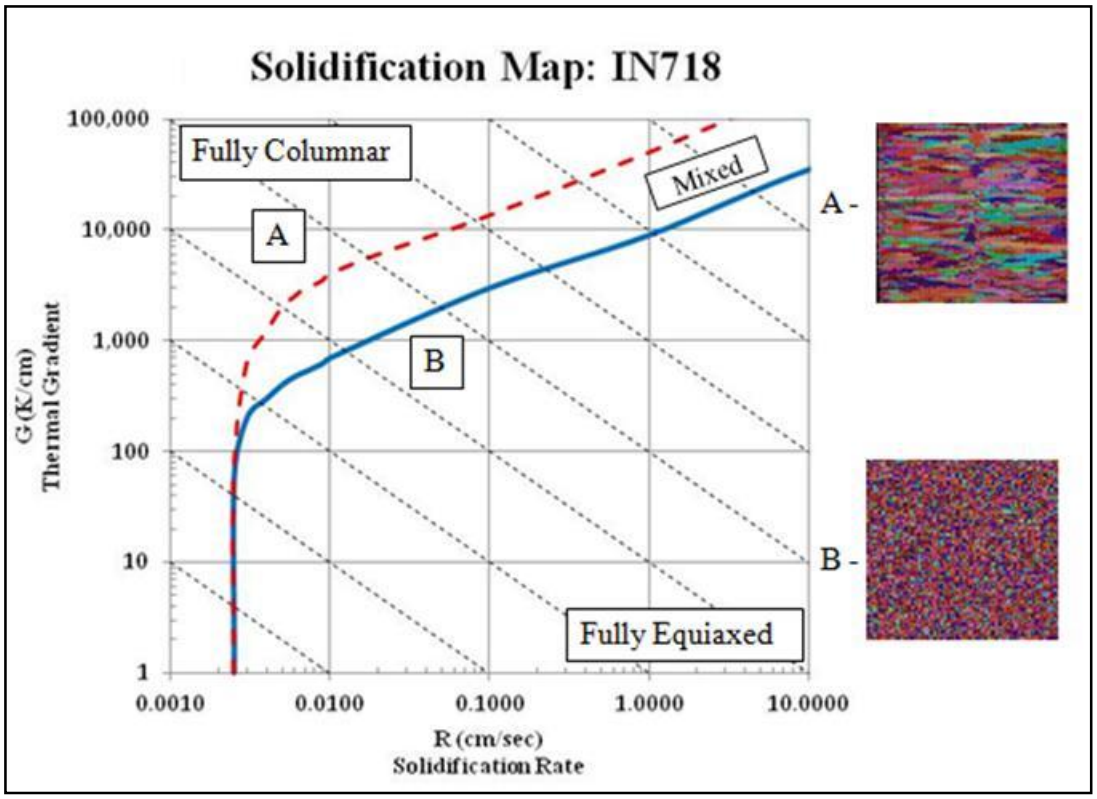

Figure 3.5.1 – Verification of solidification accuracy

Chapter 4. Inconel® Alloy 718 Finite Element Analysis

4.1 Finite Element Analysis Model

The (FEA) model used for this research was developed by Gockel et al. [37], which was an iteration of Vasinonta's model [35] that was previously discussed. The model was constructed in Abaqus® FEA software, consisting of a bulky 3D geometry as a symmetric half model about the *x*-*z* plane, shown in Figure 4.1.1, taking temperature dependent properties along with latent heat effects into account.

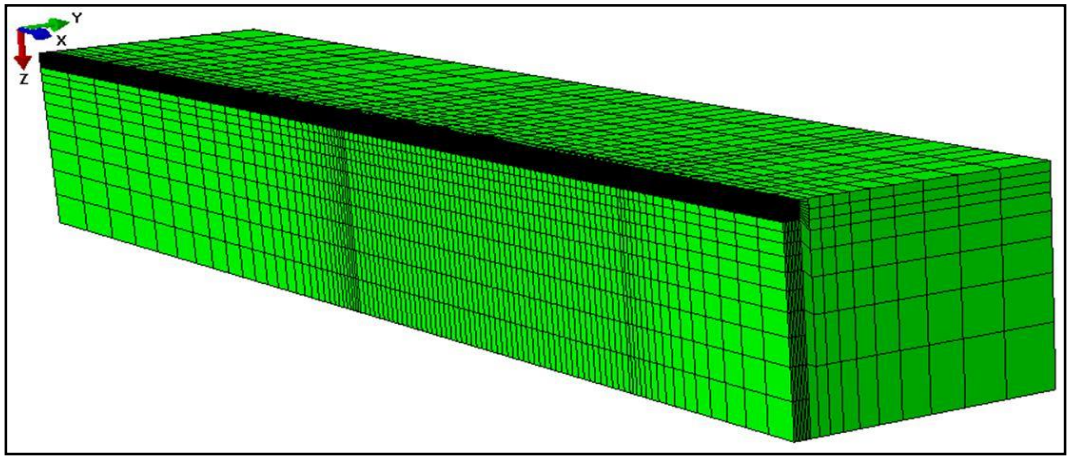

Figure 4.1.1 – 3D non-linear FEA symmetric half model

In Figure 4.1.1, the meshing of the model becomes finer toward the middle while remaining coarse on either end. This allows the melt pool to reach a steady state while keeping edge effects from altering the geometry of the melt pool [6]. This fine mesh area in Figure 4.1.2 is where melt pool data was extracted. A fine mesh ensures accuracy of results in the vicinity of the steady-state melt pool.

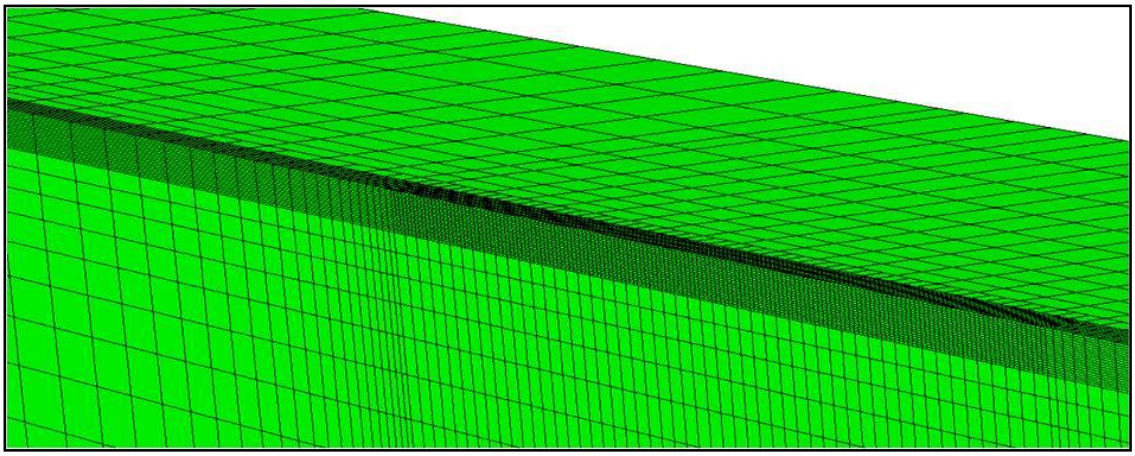

Figure 4.1.2 – Zoomed in view of fine mesh in 3D non-linear FEA symmetric half model

For this model the base plate and bottom surface had a uniform temperature of 25°C, while all other sides were considered insulated boundary conditions. This negated convection and radiation for the simulation, as it has been observed by prior researchers that the additive process is dominated by conduction [6]. The added material is represented by a 5 element by 10 element pad of inactive elements that are activated at the beginning of each step, seen in Figure 4.1.3. A heat flux corresponding to the absorbed power is then added to the activated elements shown in Figure 4.1.4. Beam velocity is held constant by adjusting step time in accordance with element size.

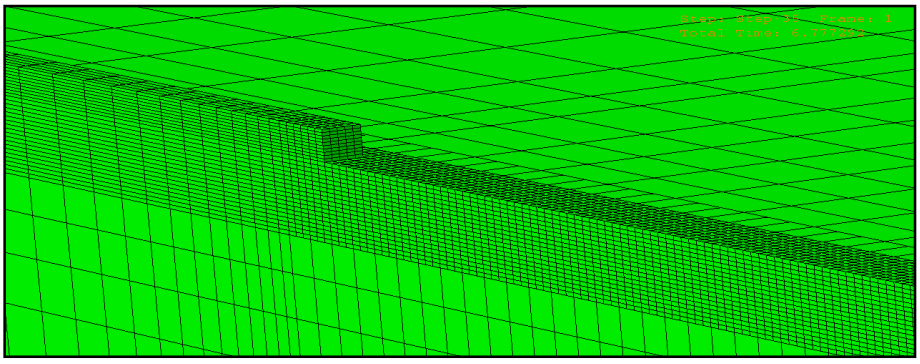

Figure 4.1.3 – Material being added as activated elements

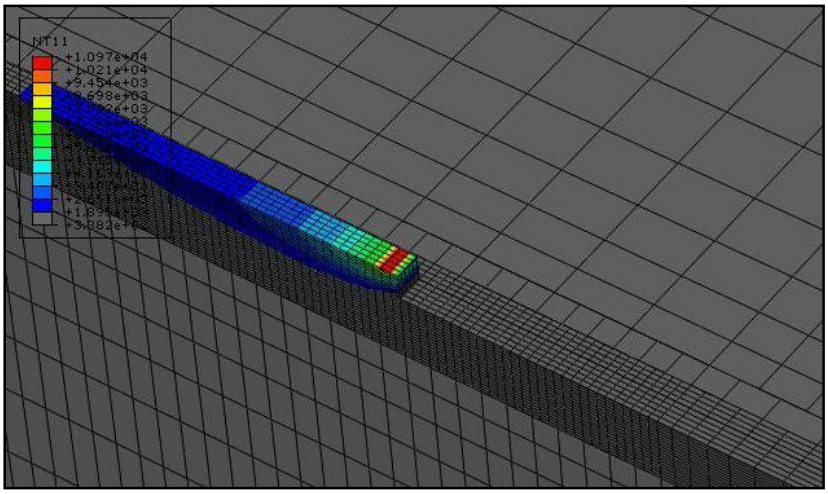

Figure 4.1.4 – Heat flux applied, representing beam power

4.2 Rosenthal Guided FEA

The Rosenthal solution for a moving point heat source can give useful insight into trends in beam-based additive manufacturing. A MATLAB® code was developed by Davis to calculate melt pool area for Ti-6Al-4V for both the 2D and 3D cases [6, 19]. When the MATLAB code runs, cooling rates, thermal gradient and melt pool depth can be extracted, all based on an initial guess of depth. For this analysis, the 3D code was used with Inconel 718 thermophysical properties set to values corresponding to 25°C and 1355°C. These properties can be found in Table 1.3.2. Rosenthal solutions matrices were constructed for specific melt pool areas – 0.016 in^2, 0.032 in^2 and 0.064 in^2. These matrices are shown in Table 4.2.1 and Table 4.2.2. This gave a first term approximation for what could be expected for melt pool depth and would be the starting points for the fully non-linear FEA models.

Power(W)	Velocity (in/min)		
10,000	184.5	92	46
9,000	166	83	41.43
8,000	147.5	73.5	36.74
7,000	129	64.5	32.05
6,000	110.5	55.15	27.37
5,000	92	45.8	22.69
4,000	73.5	36.45	18
3,000	55	27.1	13.31
2,000	36	17.63	8.31
1,000	16.85	7.68	3.089
0	0	0	0
Area →	**0.016 in^2**	**0.032 in^2**	**0.064 in^2**

Table 4.2.1 – Rosenthal results with thermophysical properties set to 25°C values

Power(W)	Velocity (in/min)		
10,000	126	62.5	30.81
9,000	113	56.1	27.5
8,000	100.35	49.6	24.19
7,000	87.7	43.1	20.89
6,000	74.6	36.5	17.5
5,000	61.5	29.9	14.05
4,000	48.4	23.09	10.51
3,000	35	16.1	6.81
2,000	21	8.7	2.87
1,000	6.01	4.06	1.05
0	0	0	0
Area →	**0.016 in^2**	**0.032 in^2**	**0.064 in^2**

Table 4.2.2 – Rosenthal result with thermophysical properties set to 1335°C values

Figure 4.2.1 and Figure 4.2.2 shows velocity along the horizontal axis with power along the vertical axis. Areas are held to constant values, showing that the same melt pool can be achieved through a range of different powers and velocities. Only the thermophysical properties in the Rosenthal solution differ between Figure 4.2.1 and Figure 4.2.2.

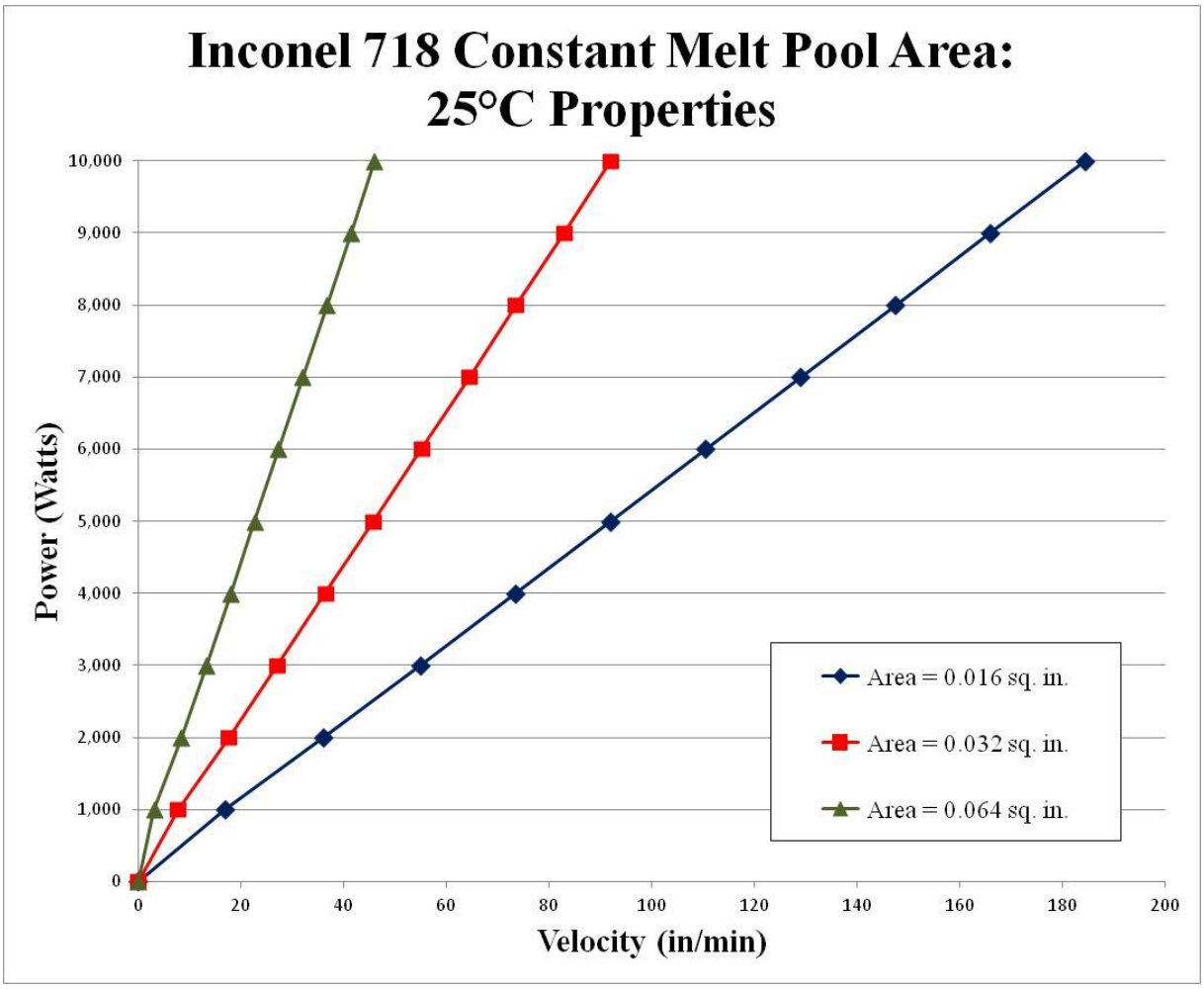

Figure 4.2.1 – Rosenthal solution lines of constant area in P vs. V space; 25°C properties

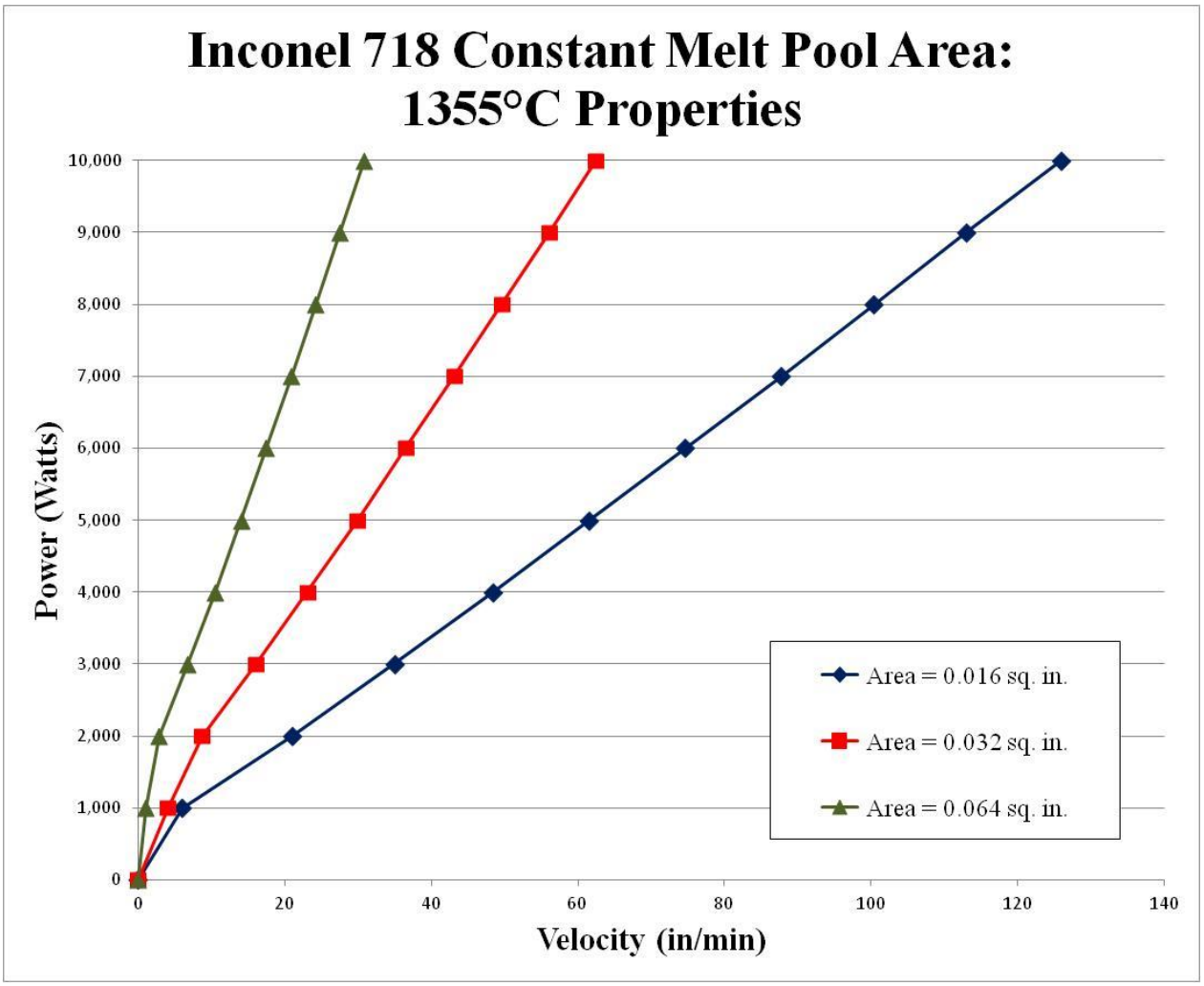

Figure 4.2.2 – Rosenthal solution lines of constant area in P vs. V space; 1335°C properties

The Rosenthal tables and plots served as a guide for non-linear FEA simulations which targeted areas of 0.016 in^2, 0.032 in^2 and 0.064 in^2 as in prior work [20, 37]. Power was held constant and velocity was varied while targeting specific areas. This iterative process was expedited largely because of the first term approximation calculated with the Rosenthal solution. Results for non-linear FEA simulations for Inconel 718 are in Table 4.2.3, showing nine data points producing 3 lines of constant area. Figure 4.2.3 has beam power in watts on the vertical axis with velocity in inches per minute along the horizontal

axis. As with the Rosenthal solution and prior work with Ti-6Al-4V, a linear relationship between power and velocity is present when area is held constant.

Power(W)	Velocity (in/min)		
10,000	198	101.3	52.57
5,000	107	54.8	29.75
1,000	29.8	19.9	7.98
0	0	0	0
Area →	0.016 in^2	0.032 in^2	0.064 in^2

Table 4.2.3 – Non-linear FEA results for Inconel718

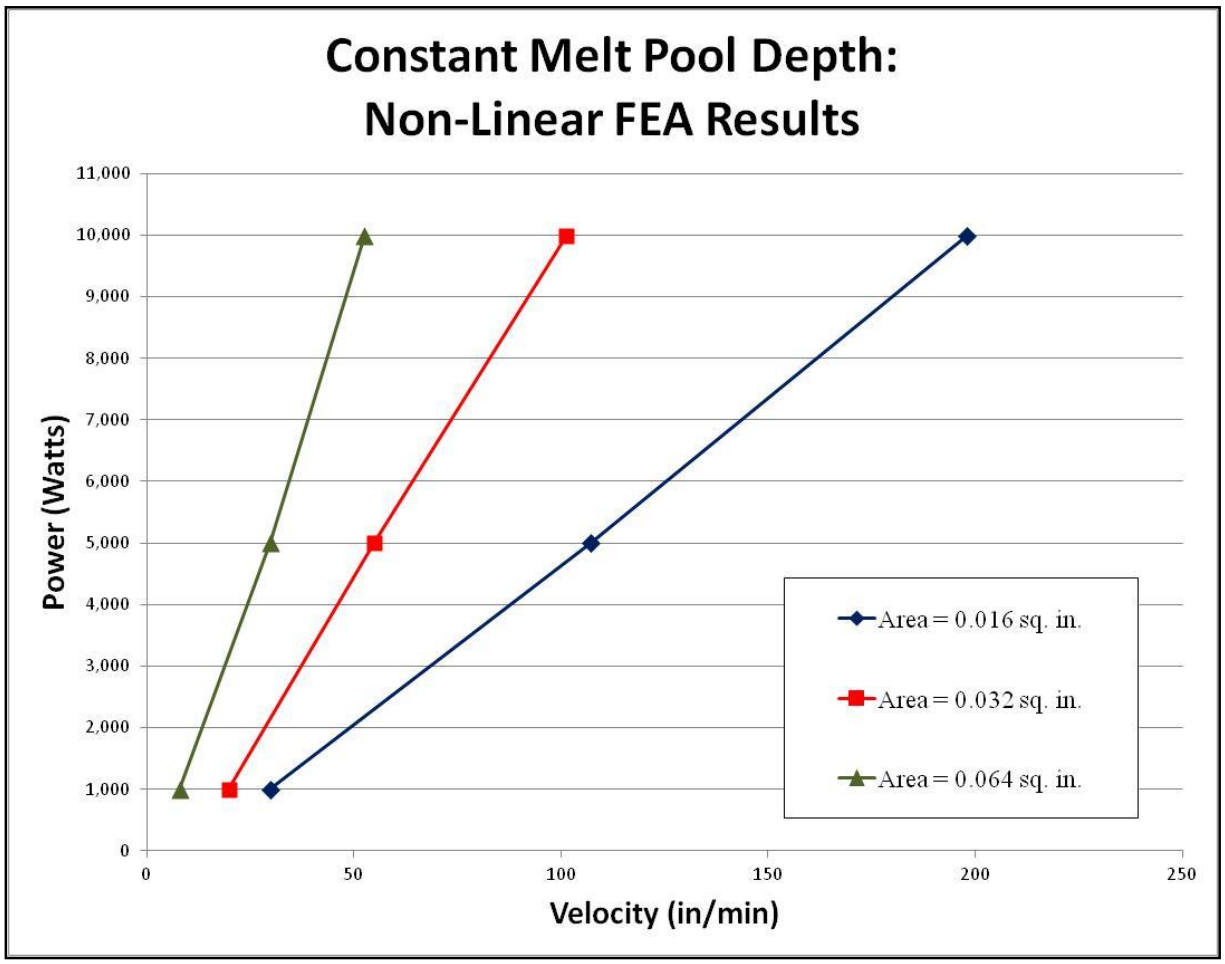

Figure 4.2.3 – Plot showing lines of constant area for Inconel 718 from non-linear FEA

4.3 Finite Element Analysis Verification

Although no experiments for additive manufacturing of Inconel 718 were made available for this thesis, similar methods were previously used to model Ti-6Al-4Vl [40]. When the added material model was compared to experimental results it was observed that the resultant areas were exactly the same for high velocity cases. Accuracy dropped when velocity was reduced and melt pool area was increased while never exceeding error greater than 25% shown in Table 4.3.1. The reduction in accuracy was due to the fact that in the high velocity cases, no preheating of the base material takes place, whereas at low velocities, the base material is affected by the heat diffusion of the electron beam [40].

Power (W)	Velocity (in/min)	Melt Pool Area		Error
		FEA	Experimental	
5,000	87.4	0.016	0.016	0.00%
3,000	52.0	0.016	0.016	0.00%
2,000	32.0	0.017	0.017	0.00%
5,000	42.5	0.033	0.032	3.13%
3,000	23.6	0.034	0.035	2.86%
2,000	13.9	0.034	0.037	8.11%
5,000	19.4	0.069	0.073	5.48%
3,000	10.9	0.068	0.079	13.92%
2,000	5.2	0.079	0.104	24.04%

Table 4.3.1 – Comparison between Ti-6Al-4V FEA and experimental melt pool areas [40]

Table 4.3.1 is represented in Figure 4.3.1 graphically, with melt pool area along the vertical axis and beam velocity on the horizontal axis, measured in in^2 and *in/min* respectively. The dashed lines with square markers represent the experimental results while the green dotted lines with the diamond markers represent the non-linear results. The colors designate the targeted melt pool area, blue for 0.016 in^2, red for 0.032 in^2 and

green for 0.064 in^2. The space between the same color lines represents the error. These results show excellent correlation in the high velocity regime, although the accuracy decreases at low velocity/large melt pool area. This shows the overall accuracy of the FEA method implemented in this research.

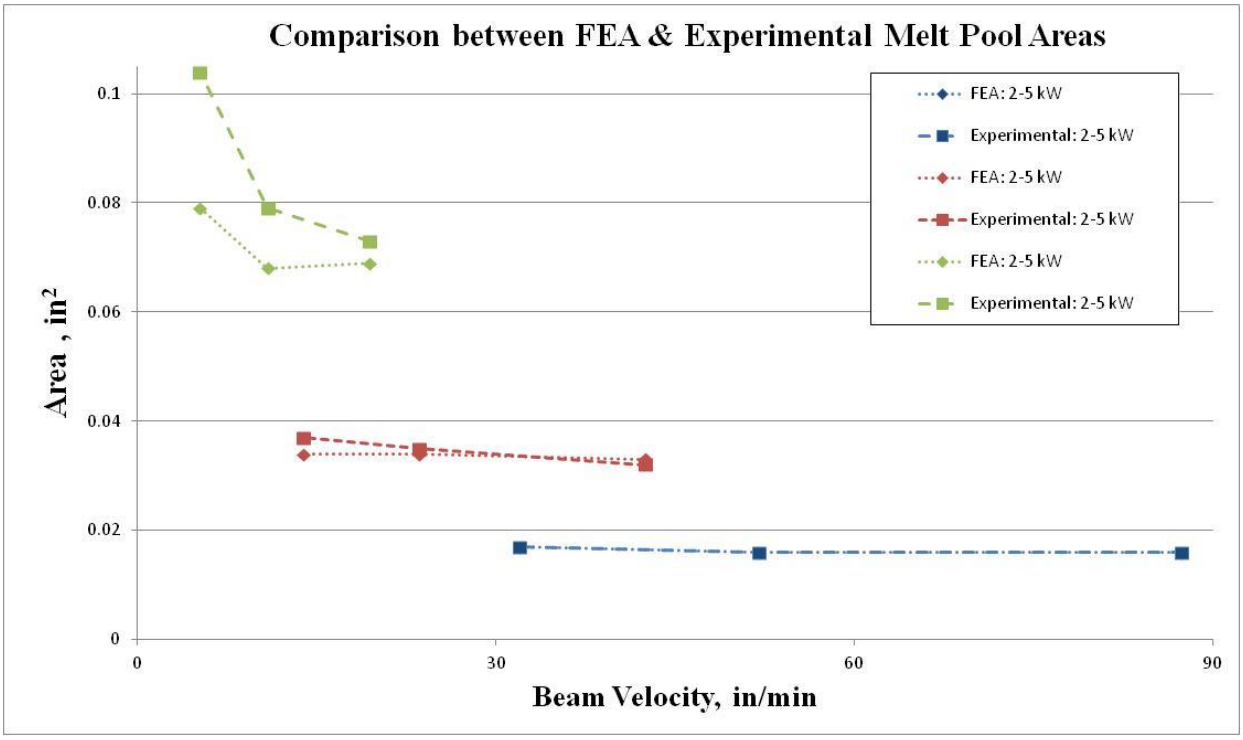

Figure 4.3.1 – Comparison between FEA and experimental melt pool area for Ti-6Al-4V: blue lines target 0.016 in2, red lines target 0.032 in2, and green lines target 0.064 in2 [40]

4.4 Combine FEA and CAFE

With confidence in both the ProCAST with CAFE and non-linear FEA simulations it was necessary to combine the results and produce a microstructure map of IN718 in power verses velocity space. In order to transform a solidification map from G vs. R space to power vs. velocity space a fitted Rosenthal approach was used, [37] as it is not computationally feasible to run fully non-linear FEA as a conversion tool. Recall that the 3D Rosenthal solution took thermophysical properties (ρ, c, k) and set them to a single

temperature value and solved for various unknowns. This gave a good first order approximation and reasonable trend predictions. However, the actual answer differs from that of a non-linear FEA as shown in Figure 4.4.1, especially at lower beam powers and velocities.

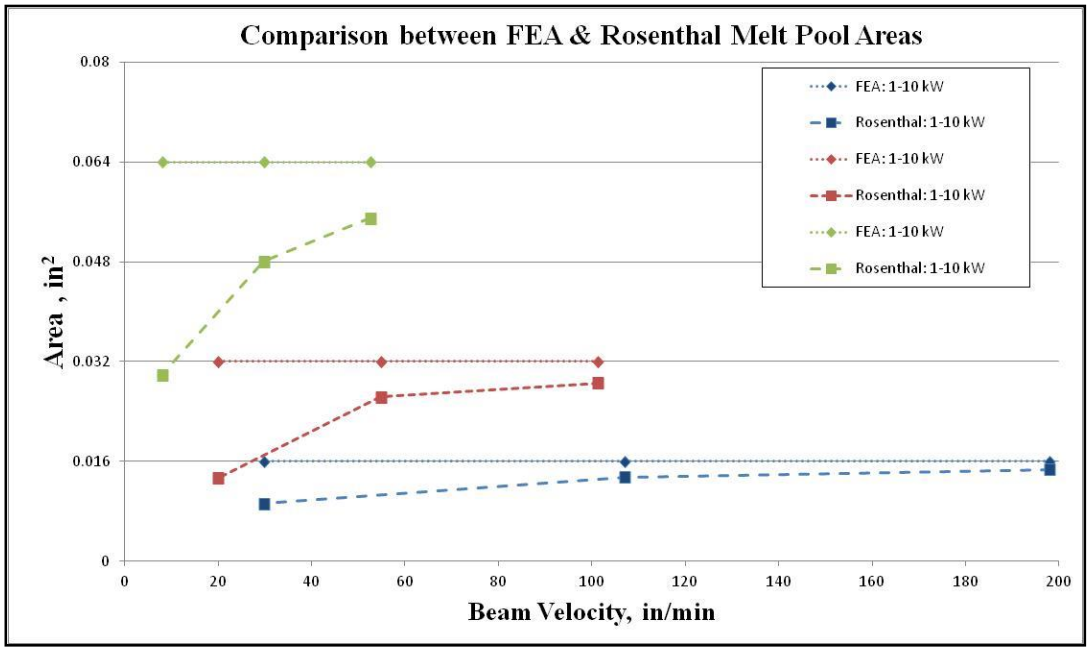

Figure 4.4.1 – Comparison between FEA and Rosenthal (20° properties) melt pool area for IN718: blue lines target 0.016 in2, red lines target 0.032 in2, and green lines target 0.064 in2

Figure 4.4.1 shows melt pool area along the vertical axis and beam velocity on the horizontal axis, measured in in^2 and in/min respectively. The dashed lines with square markers represent the Rosenthal solution results while the green dotted lines with the diamond markers represent the non-linear results. The colors designate the targeted melt pool area, blue for 0.016 in^2, red for 0.032 in^2 and green for 0.064 in^2. The space between the same color lines represents the error. The difference between non-linear FEA and Rosenthal solution were as large as 140% error, for the 0.032 in^2 at 19.90 in/min case.

This high error is expectedly from the resistance to heat flow in IN718, which is exploited at low power situations.

It was proposed by previous authors that the thermophysical properties (ρ, c, k) could be adjusted for specific power and velocity bands to match results from non-linear FEA [37]. It has been shown that the link between a non-linear FEA and a fitted Rosenthal solution melt pool geometry can be extremely accurate [40]. Figure 4.4.2 shows melt pool area along the vertical axis and beam velocity on the horizontal axis, measured in in^2 and in/min respectively. The dashed lines with square markers represent the experimental results while the green dotted lines with the diamond markers represent the fitted Rosenthal solution results. The colors designate the targeted melt pool area, blue for 0.016 in^2, red for 0.032 in^2 and green for 0.064 in^2. The space between the same color lines represents the error. For the high velocity cases the accuracy is nearly 100% and does not start to diverge until beam velocity drops below 30 in/min [40].

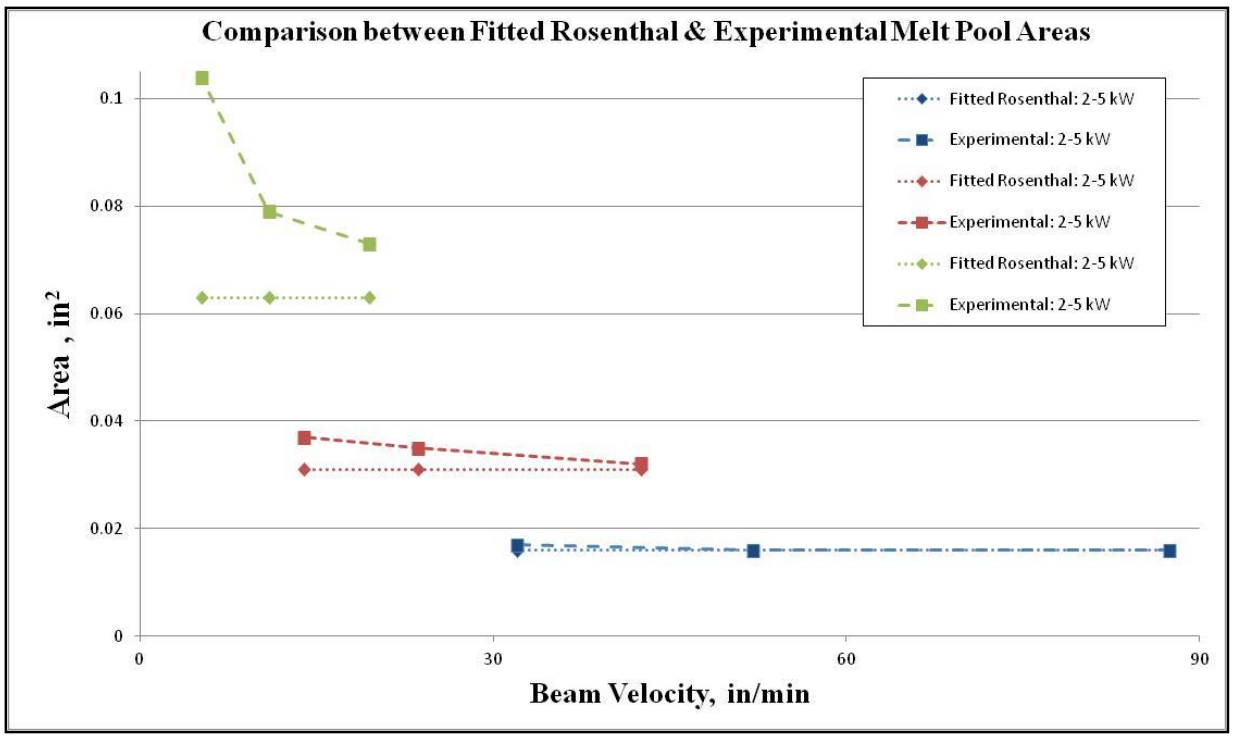

Figure 4.4.2 – Comparison between fitted Rosenthal and experimental melt pool area for Ti-6Al-4V: blue lines target 0.016 in2, red lines target 0.032 in2, and green lines target 0.064 in2 [40]

A series of fitted Rosenthal solution runs were executed in MATLAB scripts. Beam absorbed power (αQ) and velocity (V) were inputs, the outputs were thermal gradient (G) and cooling rate, which was converted to solidification rate (R) with Eq. 2.5.1. These outputs were then plotted on the verified solidification map for IN718. If the point landed on the morphology boundary line, the power and velocity were recorded. If the point did not intersect the morphology boundary lines, the method was repeated with power and/or velocity adjusted. This method was repeated for each power (1-6kW) until all values intersected the morphology boundaries. It was then repeated for the next power level. Once each designated power level had points on both boundaries they were plotted as shown in Figure 4.4.3.

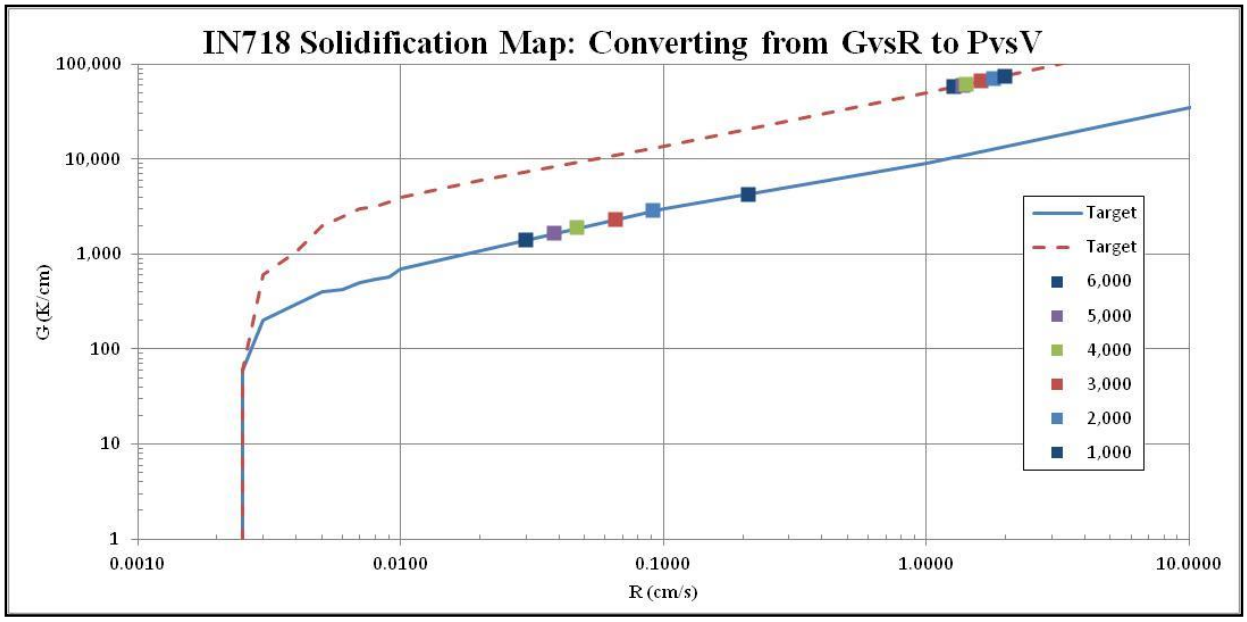

Figure 4.4.3 – Conversion plot from G vs R to P vs V space for IN718 – power in watts

To finish converting grain morphology boundaries from G *vs.* R space to P *vs.* V space, the powers and velocities that produced points of intersection in Figure 4.4.3 were plotted in P *vs.* V space. Those points were connected with a smooth curve fit and the boundaries were converted from a solidification plot for IN718 in G *vs.* R space to process map for IN718 in P *vs.* V space. Similarly to previous authors the slopes of lines of constant area were taken with a y-intercept of 0 and represent lines of constant grain size for IN718 [20]. Figure 4.4.4 is the first process map for IN718 in P *vs.* V space with absorbed beam power along the vertical axis and beam velocity on the horizontal axis. Below the red dashed line the microstructure is expected to be fully columnar, while above the blue solid line the microstructure is expected to be fully equiaxed, with a mixed morphology between the lines. Figure 4.4.5 show the link between melt pool geometry and solidification microstructure as it pertains to beam based additive manufacturing of IN718.

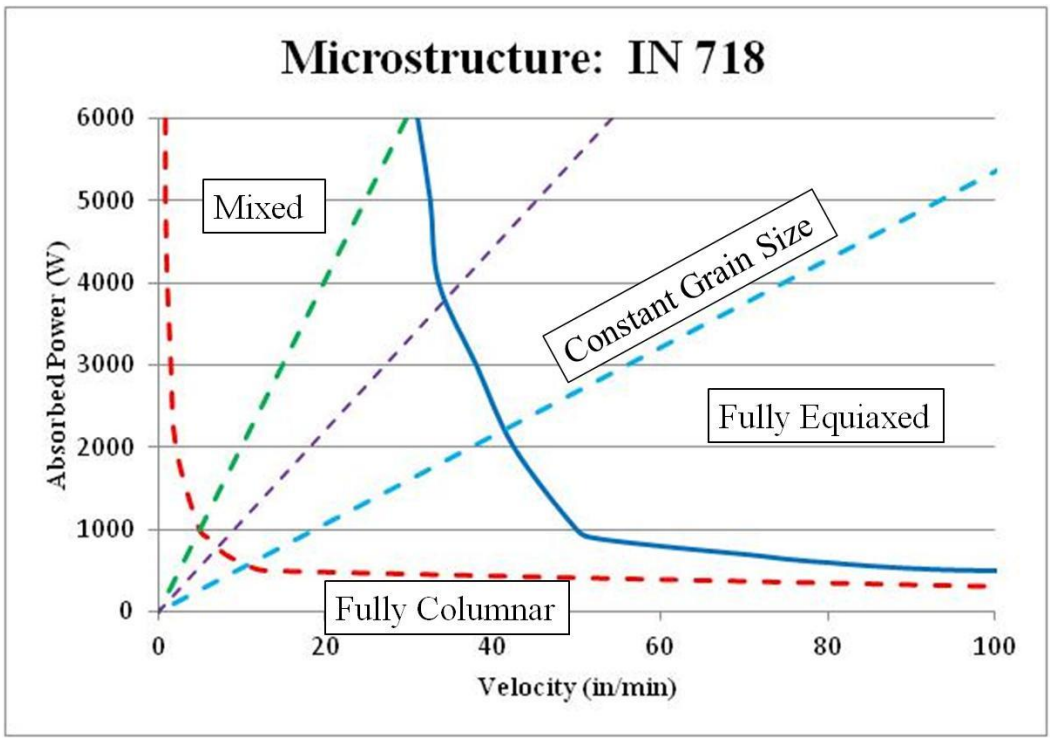

Figure 4.4.4 – Process map for microstructure prediction of IN718 in absorbed power verses velocity space

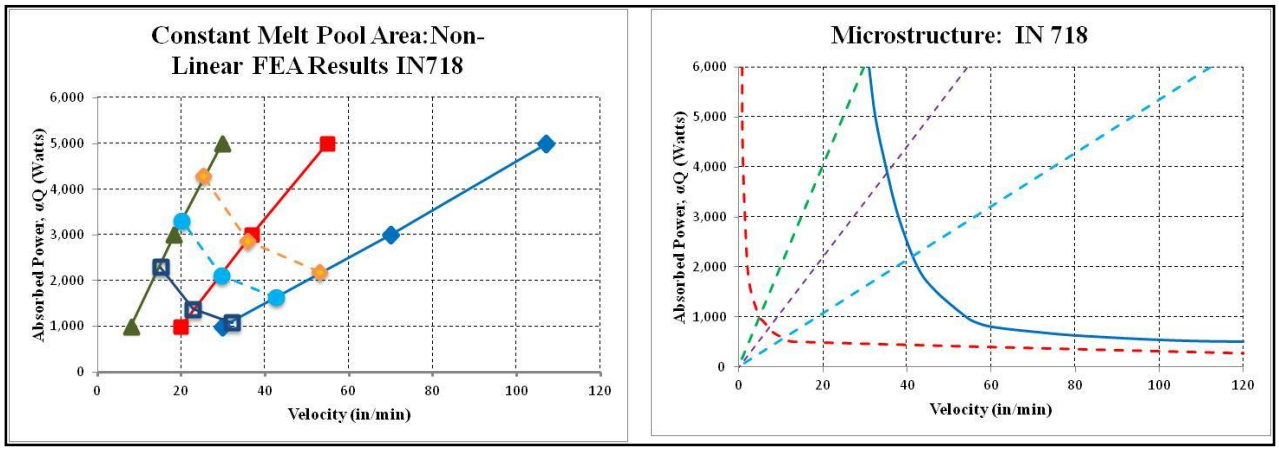

Figure 4.4.5 – Link between melt pool geometry and microstructure for IN718

Chapter 5. Results and Contributions

5.1 Summary of Results

Throughout this thesis, many methods that were previously implemented in the research of Ti-6Al-4V as it pertains to additive manufacturing were used, showing those previous developed methods are not limited to Ti-6Al-4V. As this research was modeled after the work accomplished by Davis [6, 20, 37], it was critical to understand the Rosenthal solution for quickly calculating a first order approximation and predicting trends. Equally as important as the Rosenthal solution, it was necessary to understand solidification maps and to acquire or create one for IN718. Since the literature review revealed only one solidification map for IN718, it was determined that the solidification map would need to be confirmed. ProCAST with CAFE was used to confirm the previously published solidification map for IN718. The software was used to validate the acquired solidification map by checking microstructure in the equiaxed and columnar regions.

Rosenthal solutions were then used to guide a series of targeted non-linear 3D additive manufacturing FEA runs to produce lines of constant area in power verses velocity space. Converging on three separate lines of constant area was an iterative process that took 37 individual runs, taking between 12-30 hours, running between 3 machines. Having these lines of constant area and length over depth ratio enabled comparison to Ti-6Al-4V results. The non-linear results proved what the preliminary Rosenthal results suggested, that changing alloy systems was simply changing material properties (ρ,c,k) and shifts those lines in power verses velocity space.

Producing a design space (P *vs.* V) microstructure map with morphology regions was rooted back to understanding the Rosenthal solution. Instead of inputting the powers

and velocities and extracting a melt pool area, the desired melt pool was known along with the power and velocity. Thermophysical properties were adjusted to match non-linear FEA, hence the fitted Rosenthal solution. Once these parameters were determined, they were used to iterate through powers and velocities to produce thermal gradients and cooling rates that correspond to the morphology regions defined on the verified solidification map.

5.2 Contributions

The contributions of this thesis include the following:

1. Expanded existing methods in place for Ti-6Al-4V to other alloy system as it pertains to additive manufacturing solidification microstructure.
2. Validate previously published solidification microstructure maps in G vs. R space for IN718 using CAFE simulations.
3. Used 3D non-linear FEA guided by the 3D Rosenthal solution to produce a previously unpublished PV process map for solidification microstructure in beam-based additive manufacturing of IN718.

This work confirms that the methods used in previous research with Ti-6Al-4V were not alloy specific and that it translates to different alloy systems. It also shows that changing an alloy system is little more that adjusting thermophysical properties, which effectively moves the processing space – giving an extra degree of change when it comes to design. This is the first step in attempting to integrate the control of melt pool geometry and microstructure by directly controlling process variables.

5.3 Future Work

There are several aspects of this project that could be explored in the future. A comparison between the results present in this thesis could be compared to experimental deposits of IN718. Experimental results would not only confirm the results in the research, but further confirm the potential for integrated control of melt pool geometry and microstructure in additive manufacturing. The effects of preheating and reheating as it pertains to the formation of laves in the microstructure is also an area for further study, as they are formed form long exposure to heat and/or extremely slow cooling rates. This may have consequence for Arcam and other additive processes which maintain high ambient temperature during deposition.

Bibliography

[1] Amazing AM, LLC., "Additive Manufacturing [AM]," 12 2013. [Online]. Available: http://additivemanufacturing.com/. [Accessed 29 12 2013].

[2] S. Bontha, *The Effect of Process Variables on Microstructure in Laser Deposited Materials*, Ph.D. Disseration,Wright State University, 2006.

[3] Create It Real Aps, "Create It Real," 1 12 2013. [Online]. Available: http://www.createitreal.com/index.php/technology/process. [Accessed 1 12 2013].

[4] EOS, "E-Manufacturing Solutions," 17 11 2013. [Online]. Available: http://www.eos.info/additive_manufacturing/for_technology_interested. [Accessed 29 11 2013].

[5] I. Gibson, D. W. Rosen and B. Stucker, in *Additive Manufacturing Technologies*, Verlag, Springer, 2010, pp. 1-2.

[6] J. E. Davis, *Effect of Free-Edges on Melt Pool Geometry and Solidification Microstructure in Beam-Based Fabrication Methods,* M.S. Thesis,Wright State University, 2010.

[7] C. Chua, K. Leong and C. Lim, in *Rapid Prototyping: Principles and Applications*, World Scientific Publishing, 2003.

[8] K. M. Taminger and R. A. Hafley, "Electron Beam Freeform Fabrication (EBF3) for Cost Effective Near-Net Shape Manufacturing," Langley Research Center, Hampton, VA, 2006.

[9] D. Lineberry, "NASA," 22 June 2011. [Online]. Available:

http://www.nasa.gov/topics/technology/features/ebf3.html. [Accessed August 2012].

[10] Arcam, "Cad to Metal Arcam AB," 17 6 2013. [Online]. Available: http://www.arcam.com/. [Accessed 17 6 2013].

[11] S. Bontha, N. Klingbeil, P. Kobryn and H. Fraser, "Effects of Process Variables and Size-scale on Solidification Microstructure in Beam-based Fabrication of Bulky 3D Structures," *Material Science and Engineering A,* no. 513-514, pp. 311-318, 2009.

[12] R. Dykhuizen and D. Dobranich, "Analytical Thermal Models for the LENS Process," Sandia National Laboratories Internal Report, Albuquerque, 1998.

[13] R. Dykhuizen and D. Dobranich, "Cooling Rates in the LENS Process," Sandia National Laboratories Internal Report, Albuquerque, 1998.

[14] R. Dykhuizen and D. Dobranich, "Scoping Thermal Calculations of the LENS Process," Sandia National Laboratories Internal Report, Albuquerque, 1998.

[15] S. Bontha, N. W. Klingbeil, P. A. Kobryn and H. L. Fraser, "Thermal Process Maps for Predicting Solidification Microstructure in Laser Fabrication of Thin-Wall Structures," *Journal of Materials Processing Technology,* pp. 135-142, 2006.

[16] C. J. Brown, *Modeling of Solidification Microstructure in Laser-Deposited Ti-6Al-4V,* M.S. Thesis,Wright State University, 2003.

[17] P. Kobryn and M. E. H., "The Effect of Laser Power and Transverse Speed on Microstructure, Porosity and Building Height in Laser-Deposited Ti-6Al-4V," *Scripta Materialia,* 2000.

[18] P. Kobryn and S. Semiatin, "Microstructure and Texture Evolution During Solidification Procssing of Ti-6Al-4V," *Journal of Materials Processing*

Technology, pp. 330-339, 2003.

[19] H. N. Doak, *Effect of Process Variable on Sub-Melt Thermal Behavior and Solid-State Phase Transformations in Beam Based Additive Manufacturing of Ti-6Al-4V,* M.S. Thesis,Wright State University, 2013.

[20] J. Davis, J. Beuth, N. Klingbeil, B. Walker and K. Taminger, "Toward Integrated Control of Melt Pool Dimensions and Microstructure in Electron Beam Additive Manufacturing," in *Materials Sciences & Technology*, Columbus, 2011.

[21] J. Beuth, ""Process Mapping for Qualification Across Multiple Direct Metal Additive Manufacturing Processes," in *Solid Freeform Fabrication Symposium*, Austin, TX, 2013.

[22] C. Huanga, T. Wang, C. Lee and W. Hanb, "A study of the heat-affected zone (HAZ) of an Inconel 718 sheet welded with electron-beam welding (EBW)," *Materials Science and Engineering,* pp. 275-281, 2005.

[23] L. WANG, Y. YAO, J. DONG and M. ZHANG, "Effect of Cooling Rates on Segregation and Density Variation in the Mushy Zone during Solidification of Superalloy Inconel 718," *Chemical Engineering Communications*, pp. 1571-1585, 2010.

[24] L. Nastac, J. J. Valencia, M. L. Tims and F. R. Dax, "Advances in the Solidification of IN718 and RS5 Alloys," in *Superalloys 718, 625, 706 and Various Derivatives* , San Diego, 2001.

[25] Special Metals, "Inconel(R) alloy 718," Special Metals Corporation, New Hartford, NY, 2007.

[26] D. Ahn, K. Byun and M. Kang, "Thermal Characteristics in Cutting of Inconel 718 Superalloy Using CW Nd:YAG Laser," *Journal of Medical Science and Technology,* no. 26(4), pp. 362-366, 2010.

[27] B. Yilbas, S. Akhtar and C. Karatas, "Laser Surface Treatment of Inconel 718 Alloy: Thermal Stress Analysis," *Optcs and Lasers in Engineering,* vol. 48, no. 7-8, pp. 740-749, 2010.

[28] K. Amato, G. S.M., L. Murr, E. Martinez and P. Shindo, "Microstructures and mechanical behavior of Inconel 718 fabricated," *Acta Materialia,* pp. 2229-2239, 2012.

[29] The Bodner Group, "Unit Cells," Division of Chemistry Education, Purdue University, [Online]. Available: http://chemed.chem.purdue.edu/genchem/topicreview/bp/ch13/unitcell.php. [Accessed 26 January 2014].

[30] Y. Murata, M. Morinaga, N. Yukawa, H. Ogawa and M. Kato, "Solidification Structures of Inconel 718 with Microalloying Elements," in *Superalloys 718, 625, 706 and Various Derivatives*, 1994.

[31] Bertram, Minisandram and Yu, Modeling for Casting and Solidification Processing, K. Yu, Ed., New York: Marcel Dekker Inc., 2002, pp. 586-590.

[32] J. J. Schirra, R. H. Caless and R. W. Hatala, "The Effect of Laves Phase on the Mechanical Properties of Wrought and Cast + HIP Inconel 718," in *Superalloys 718, 625 and Various Derivatives*, 1991.

[33] D. W. J. Tanner, *Life Assessment of Welded Inconel 718 at High Temperature,*

University of Nottingham, 2009.

[34] D. Rosenthal, "The Theroy of Moving Sources of Heat and its Application to Metal Treatments," *Transactions of the American Society of Mechanical Engineers,* vol. 68, pp. 849 - 866, 1946.

[35] A. Vasinonta, *Process Maps for Melt Pool Size and Residual Stress in Laser-Based Solid Freeform Fabrication,* Ph.D. Dissertation,Carnegie Mellon University, 2002.

[36] A. Vasinonta, M. Beuth and M. Griffith, "Process Maps for Laser Deposition of Thin-walled Structures," in *Solid Freeform Fabrication Symposium*, Austin, TX, 1999.

[37] J. Gockel, *Integrated Process Mapping of Solidification Microstructure and Melt Pool Dimensions in Additive Manufacturing of Ti-6Al-4V,* Ph.D. Dissertation,Carnegie Mellon University, 2014.

[38] ESI, "ESI-Group," ESI, 12 December 2013. [Online]. Available: https://www.esi-group.com/software-services/virtual-manufacturing/casting. [Accessed 12 December 2013].

[39] R. M. Forbes Jones and L. A. Jackman, "The Structural Evolution of Superalloy Ingots During Hot Working," *JOM,* vol. 51, no. 1, pp. 27-31, 1999.

[40] E. Soylemez, J. L. Beuth and K. Taminger, "Controling Melt Pool Dimensions Over a Wide Range of Material Deposition Rates in Electron Beam Additive Manufacturing," in *Solid Freeform Fabrication,* Austin, 2010.

[41] J. F. Radavich, "The Physical Metallurgy of Cast and Wrought Alloy 718," in *Superalloy 718 - Metallugry and Applications*, 1989.

[42] K. Bird and J. Hibberd, "Tensile Properties and Microstructure of Inconel 718 Fabricated with Electron Beam Freeform Fabrication (EBF3)," National Aeronautics and Space Administration, Hampton, Virginia, 2009.

[43] Z. Xiaoming, C. Jing, L. Xin and H. Weidong, "Study on Microstructure and Mechanical Properties," *Materials Science and Engineering*, pp. 119-124, 2008.

[44] P. Gao, K.-f. Zhang, B.-g. Zhang, J. Shao-Song and Z. Bao-Wei, "Microstructures and High Temperature Mechanical Properties of Electron Beam Welded Inconel 718 Superalloy Thick Plate," *Transactions of Nonferrous Metals Society of China*, pp. 315-322, 2011.

[45] F. Liu, X. Lin, G. Yang, M. Song, J. Chen and W. Huang, "Microstructure and Residual Stress of Laser Rapid Formed Inconel 718 Nickel-base Superalloy," *Optics & Laser Technology*, pp. 208-213, 2011.

[46] G. D. Janaki Ram, A. V. Reddy, K. P. Rao and G. M. Reddy, "Microstructure and Mechanical Properties of Inconel 718 Electron Beam Welds," *Materials Science and Technology*, pp. 1132-1138, 2005.

[47] F. Liu, X. Lin, H. Leng, J. Cao, Q. Liu, C. Huang and W. Huang, "Microstructural Changes in a Laser Solid Forming Inconel 718 Superalloy Thin Wall in the Deposition Direction," *Optics & Laser Technology*, pp. 330-335, 2013.

[48] L. E. Murr, S. M. Gaytan, D. A. Ramirez, E. Martinez, J. Hernandez, K. N. Amato, P. W. Shindo, F. R. Medina and R. B. Wicker, "Metal Fabrication by Additive Manufacturing Using Laser and Electron Beam Melting Technologies," *Journal of Material Science and Tehnology*, pp. 1-14, 2012.

[49] W. Kurz, C. Benzençon and M. Gäumann, "Columnar to Equiaxed Transition in Solidification Processing," *Science and Technology of Advanced Materials*, pp. 185-191, 2001.

[50] H. Kitaguchi, "Microstructure-Property Relationship in Advanced Ni-Based Superalloys," in *Advances in Materials and Processes*, Rijeka, Croatia, InTech Europe, 2012, pp. 19-41.

[51] S.-C. Lee, S.-H. Chang, T.-P. Tang, H.-H. Ho and J.-K. Chen, "Improvement in the Microstructure and Tensile Properties of Inconel 718 Superalloy by HIP Treatment," *Materials Transactions, The Japan Institute of Metals*, pp. 2877-2881, 2006.

[52] K. N. Amato, J. Hernandez, L. E. Murr, E. Martinez, S. M. Gaytan and P. W. Shindo, "Comparison of Microstructures and Properties for a Ni-Base Superalloy (Alloy 625) Fabricated by Electron and Laser Beam Melting," *Journal of Materials Science Research* , pp. 4-41, 2012.

[53] J. Milewski, P. Dickerson, R. Nemec, G. Lewis and J. Fonseca, "Application of a manufacturing model for the optimization of additive processing of Inconel alloy 690," *Journal of Materials Processing Technology*, pp. 18-28, 1999.

[54] A. Nunes, "An Extended Rosenthal Weld Model," *Welding Research Supplement*, pp. 165-s - 170-s, 1983.

[55] L. Murr, E. Martinez, S. Gaytan, D. Ramirez, B. Machado, P. Shindo, J. Martinez, F. Medina, J. Wooten, D. Ciscel, U. Ackelid and R. Wicker, "Microstructural Architecture, Microstructures, and Mechanical Properties for a Nickel-Base Superalloy Fabricated by Electron Beam Melting," *The Minerals, Metals &*

Materials Society and ASM International, pp. 3491-3808, 2011.

[56] D. R. Gaddam, *Three-Dimensional Modeling of Melt-Pool Geometry and Solidification Microstructure in Laser Deposited Ti-6Al-4V,* M.S. Thesis, Wright State University, OH, 2005.

APPENDIX A: 3D MATLAB Script

```
% Fitted 3D Cooling

% Run before 3D Rosenthal Solution

% Created by Joy Davis

% Modified by John Thompson

clc

clear all

%Note Q is alphaQ

Q=10000;

% Velocity = (inches per min) * convert to m/s

v=30.81*4.2333418000169E-4;

% Initial guess for root finding

x0bar(1)=-1;

% Resolution 10,000 normally

A=10000;

% Normalized melt pool depth

ND = -15;

% IN718 Material Properties at 25C

% rho=8144 ;    %Density

% c=428.05;    %Specific Heat

% k=11.5;      %Thermal Conductivity

% IN718 Material Properties at 1355C

rho = 7294;    %Density

c = 692.74;    %Specific Heat

k = 31.4;      %Thermal Conductivity

% rho = 6700;   %adjusted density

% c = 427.14;    %adjusted Specific Heat

% k = 11.4;      %adjusted Thermal Conductivity

Tm = 1335;     % Melting Temperature C

T0 = 25;      % Temperature of the Base Plate C
```

```
out=[];
Tmbar = ((Tm - T0)/(((Q)/(pi*k))*((rho*c*v)/(2*k))))
% Variance of Normalized melt pool length (0 < d < L)
d = linspace(0 ,ND, A);
D = d';
% Initializations
t = 1;
m = 1;
n = 1;
while n <= A
    z0bar(m) = D(m);
    y0bar(m) = 0;
    x(m) = fzero(@f3d,x0bar(m),[],Tmbar,z0bar(m));
    cterm1(m) =((exp(-(x(m)+sqrt(x(m)^2+y0bar(m)^2+z0bar(m)^2))))/...
        (sqrt(x(m)^2+ y0bar(m)^2+ z0bar(m)^2))
    bcterm1(m) = (x(m)/sqrt(x(m)^2+y0bar(m)^2+z0bar(m)^2));
    bcterm2(m) = (x(m)/(x(m)^2+y0bar(m)^2+z0bar(m)^2));
    NCR(m) = 0.5*cterm1(m)*(1+bcterm1(m)+bcterm2(m));
    CR(m) = abs(NCR(m))/(((2*k)/(rho*c*v))^2*((pi*k)/(Q*v)));
    x0bar(m+1)=x(m);
    z0(m)=z0bar(m)/ND;
    m=m+1;
    n=n+1;
end
disp('hi')
% Fitted 3D Rosenthal Solution
% Created by Joy Davis
% Modified by John Thompson
% Value of Tmbar
clc
% Definition of constants
```

```
siz=size(z0bar);

n=siz(2);

%x0bar(2) from cooling

          tmpx0bar= x0bar(2);

          tmpnd= z0bar(n-1);

clear x0bar z0bar y0bar x cterm1 bcterm1 bcterm2

clear A D NCR ND d m n t z0 CR

out=[];

%V=((Tm-T0)*(2*k^2*pi))/(Tmbar*rho*c*Q)

tmpLP =[Q];

%a = input('Input the value of "a" (distance from free edge) = ');

for i=1:(size(tmpLP))%1

    Q=tmpLP(i);

    Tmbar = ((Tm - T0)/(((Q)/(pi*k))*((rho*c*v)/(2*k))))

    %input('Please input the value of Tmbar = ');

    % Initial guess for root finding found with program "cooling"

    x0bar(1) = tmpx0bar(i);

    %input('Please input the initial guess for root finding = ');

    % Resolution

    A = 20;

    ND = tmpnd(i)

    %input('Please input the melt pool depth = ');

    %ND =  0.16383762376238;

    % Variance of Normalized melt pool length (0 < d < L)

    d = linspace(0,ND,A);

    D = d';

    % Initializations

    t = 1;

    m = 1;

    n = 1;

while n <= A
```

```
z0bar(m) = D(m);

y0bar(m)=0;

x(m) = fzero(@f3d,x0bar(m),[],Tmbar,z0bar(m));

T(m)=exp(-(x(m)+sqrt(x(m)^2+y0bar(m)^2+z0bar(m)^2)))/(2*...
     sqrt(x(m)^2+y0bar(m)^2+z0bar(m)^2));
 % Non-dimensional Cooling Rate
cterm1(m) =((exp(-(x(m)+sqrt(x(m)^2+y0bar(m)^2+z0bar(m)^2))))/...
     (sqrt(x(m)^2+ y0bar(m)^2+ z0bar(m)^2)));
bcterm1(m) = (x(m)/sqrt(x(m)^2+y0bar(m)^2+z0bar(m)^2));
bcterm2(m) = (x(m)/(x(m)^2+y0bar(m)^2+z0bar(m)^2));
NCR(m) = 0.5*cterm1(m)*(1+bcterm1(m)+bcterm2(m));
 % Dimensional Cooling Rate
CR(m) = (abs(NCR(m)))/(((2*k)/(rho*c*v))^2*((pi*k)/(Q*v)));
%ThermX(m)= (exp(-(x(m)+sqrt(x(m)^2+z0bar(m)^2)))/...
%     (2*sqrt(x(m)^2+z0bar(m)^2)))*(1+(x(m)/sqrt(x(m)^2+z0bar(m)^2))+...
%     (x(m)/(x(m)^2+z0bar(m)^2)));
ThermX(m)= 1/2*(-1-1/(x(m)^2+z0bar(m)^2)^(1/2)*x(m))*...
     exp(-x(m)-(x(m)^2+z0bar(m)^2)^(1/2))/(x(m)^2+z0bar(m)^2)^...
     (1/2)-1/2*exp(-x(m)-(x(m)^2+z0bar(m)^2)^(1/2))/(x(m)^2+...
     z0bar(m)^2)^(3/2)*x(m);
ThermY(m)=0;
ThermZ(m)=-1/2/(x(m)^2+z0bar(m)^2)*z0bar(m)*exp(-x(m)-(x(m)^2+...
     z0bar(m)^2)^(1/2))-1/2*exp(-x(m)-(x(m)^2+z0bar(m)^2)^(1/2))/...
     (x(m)^2+z0bar(m)^2)^(3/2)*z0bar(m);
%ThermZ(m)= -(((z0bar(m)*exp(-(x(m)+sqrt(x(m)^2+z0bar(m)^2))))/...
%     (2*(x(m)^2+z0bar(m)^2)))*(1+(1/(sqrt(x(m)^2+z0bar(m)^2)))));
 % Non-dimensional Thermal Gradient
 NTG(m) = sqrt((ThermX(m))^2+ (ThermZ(m))^2);
 % Dimensional Thermal Gradient
 G(m)=(abs(NTG(m))/(((2*k)/(rho*c*v))^2*((pi*k)/(Q))))/100;
 % Multiplication by 100 to convert from K/m to K/cm
```

```
      NR(m) = (abs(NCR(m))/abs(NTG(m)));
      R(m)= CR(m)/G(m);
      %FOr solidification at the edge
      xObar(m+1) = x(m);
      zO(m) = zObar(m)/ND;
      %Non dimensional x0 for plot
      xO(m)= x(m)/ -tmpxObar;
      m = m + 1;
      n = n + 1;
 end
 %Out = [x' zO' abs(NCR') NTG'];
  TempDepth(:,i)=zObar';
  TempTmbar(:,i) = Tmbar';
  TempG(:,i)= abs(G');
  TempCR(:,i)= abs(CR');
end
for p=1:(size(tmpLP))
         z=1;
        for j=1:200:A
            Depth(z,p)= TempDepth(j,p);
            FCR(z,p)= TempCR(j,p);
            FG(z,p) = TempG(j,p);
          z=z+1;
      end
end
D = (abs(ND)*2*k)/(rho*c*v);
DepthInches = D*39.3701
%a = (pi*D^2)/2;% Meters^2;
Area = (pi*DepthInches^2)/2%in^2
Q
vel = v/4.2333418000169E-4
```

```
CoolingRate = CR(1,19)
```

APPENDIX B: Sample Abaqus® Input Deck

```
*HEADING
 **3D Analysis
*NODE, NSET=ALLN
1,0.000000,0.000000,0.000000
2,0.000000,0.000000,0.022301
3,0.000000,0.000000,0.042372
4,0.000000,0.000000,0.060436
5,0.000000,0.000000,0.076694
.
.
.
63996, 0.084536, 0.084536, 0.388342
63997, 0.084536, 0.084536, 0.395224
63998, 0.084536, 0.084536, 0.403136
63999, 0.084536, 0.084536, 0.412229
64000, 0.084536, 0.084536, 0.422682
*NODE, NSET=YD
64001,-0.002818,0.000000,0.000000
64002,-0.002818,0.000000,0.022301
64003,-0.002818,0.000000,0.042372
64004,-0.002818,0.000000,0.060436
64005,-0.002818,0.000000,0.076694
.
.
.
75996,-0.000282,0.002818,0.388342
75997,-0.000282,0.002818,0.395224
75998,-0.000282,0.002818,0.403136
75999,-0.000282,0.002818,0.412229
76000,-0.000282,0.002818,0.422682
```

```
**
*ELEMENT, TYPE=DC3D8
1, 1, 2, 202, 201, 4961, 4962, 5162, 5161
2, 2, 3, 203, 202, 4962, 4963, 5163, 5162
3, 3, 4, 204, 203, 4963, 4964, 5164, 5163
4, 4, 5, 205, 204, 4964, 4965, 5165, 5164
5, 5, 6, 206, 205, 4965, 4966, 5166, 5165
.
.
.
56460, 73995, 73996, 20036, 20035, 75995, 75996, 24996, 24995
56461, 73996, 73997, 20037, 20036, 75996, 75997, 24997, 24996
56462, 73997, 73998, 20038, 20037, 75997, 75998, 24998, 24997
56463, 73998, 73999, 20039, 20038, 75998, 75999, 24999, 24998
56464, 73999, 74000, 20040, 20039, 75999, 76000, 25000, 24999
*NSET, NSET=DATA, GENERATE
100, 1500, 200
64100, 65900, 200
.
.
.
*ELSET, ELSET=A198, GENERATE
46712, 54672, 1990
46911, 54871, 1990
47110, 55070, 1990
47309, 55269, 1990
47508, 55468, 1990
47707, 55667, 1990
47906, 55866, 1990
48105, 56065, 1990
48304, 56264, 1990
```

48503, 56463, 1990

*ELSET, ELSET=L1, GENERATE

.

.

.

*ELSET, ELSET=L198, GENERATE

46712, 54672, 1990

**Material Properties

*MATERIAL, NAME=Inconel718

*DENSITY

8146, 292.15

8120, 372.15

8052, 527.15

7979, 772.15

7899, 1172.15

7300, 1622.15

*LATENT HEAT

250000, 1528, 1610

*SPECIFIC HEAT

427.14, 292.15

435.00, 293.15

441.74, 372.15

481.74, 572.15

521.74, 772.15

561.74, 972.15

601.74, 1172.15

691.74, 1622.15

*CONDUCTIVITY

11.4, 292.15

12.5, 372.15

14.0, 572.15

```
15.5, 772.15
21.5, 972.15
25.0, 1200
26, 1500
27, 1700
28, 1800
*SOLID SECTION, MATERIAL=INCONEL718, ELSET=ALLE
*SOLID SECTION, MATERIAL=INCONEL718, ELSET=ADDED
*INITIAL CONDITIONS, TYPE=TEMPERATURE
ALLN, 373
YD, 373
*RESTART, WRITE, overlay
*STEP, INC=10, AMPLITUDE=STEP
*HEAT TRANSFER, DELTMX=200
1e-13, 1e-12, 1e-14
*MODEL CHANGE, REMOVE
ADDED,
*END STEP
.
.
.
*MODEL CHANGE, ADD
A150,
*DFLUX, op=new
L149, s3, 982314464.628929
*OUTPUT, FIELD, variable=preselect, FREQUENCY=1000
*OUTPUT, HISTORY, variable=preselect, FREQUENCY=1000
*NODE OUTPUT, NSET=DATA
NT,
*ELEMENT OUTPUT, ELSET=EDATA
HFLM,
```

```
*END STEP
```

APPENDIX C: MATLAB Data Extraction Script

```
clc

clear matrixA

[header_mat,matrixA,j] = read_data('cutMatrix.txt');


%Test MatrixA

%matrixA = [1:3;-1,-2,-3;2:4;2:4;3:5;5:7]

%Eliminates Duplicate X values

i=2;

while i < size(matrixA,1)

    if matrixA(i,3) == matrixA(i-1,3)

        matrixA(i,:) = [];

    end


    if i > size(matrixA,1)

        break

    else

        i=i+1;

    end

end

%Eliminates Negative Z values

% i=1;

% while i < size(matrixA,1)+1

%     if matrixA(i,5) < 0

%         matrixA(i,:) = [];

%         i = i-1;

% %     end

% %

% %     if i+1 > size(matrixA,1)

% %         break

%     else
```

```
%         i=i+1;
%     end
% end
[T]=matrixA(1:size(matrixA,1),2);
[x]=matrixA(1:size(matrixA,1),3);
[y]=matrixA(1:size(matrixA,1),4);
[z]=matrixA(1:size(matrixA,1),5);
%Melt pool XZ plane
figure(1)
plot(x,-z,'o')
axis on
axis equal
hold on;
plot([min(x) max(x)], [0 0], 'k--');
%Melt cross section YZ plane
figure(2)
plot(y,-z,'o')
axis equal
hold on;
plot([min(y) max(y)], [0 0], 'k--');
%Melt pool in 3 space
% Determine the minimum and the maximum x and y values
xmin = min(x); ymin = min(y);
xmax = max(x); ymax = max(y);
% Define the resolution of the grid
xres = 200;
yres = 200;
% Define the range and spacing of the x- and y-coordinates,
% and then fit them into X and Y
xv = linspace(xmin, xmax, xres);
yv = linspace(ymin, ymax, yres);
```

```
[Xinterp,Yinterp] = meshgrid(xv,yv);
% Calculate Z in the X-Y interpolation space, which is an
% evenly spaced grid
Zinterp = griddata(x,y,z,Xinterp,Yinterp);
% Generate the mesh plot (CONTOUR can also be used)
figure(3)
mesh(Xinterp,Yinterp,-Zinterp)
colormap(cool(8))
xlabel X; ylabel Y; zlabel Z;
```